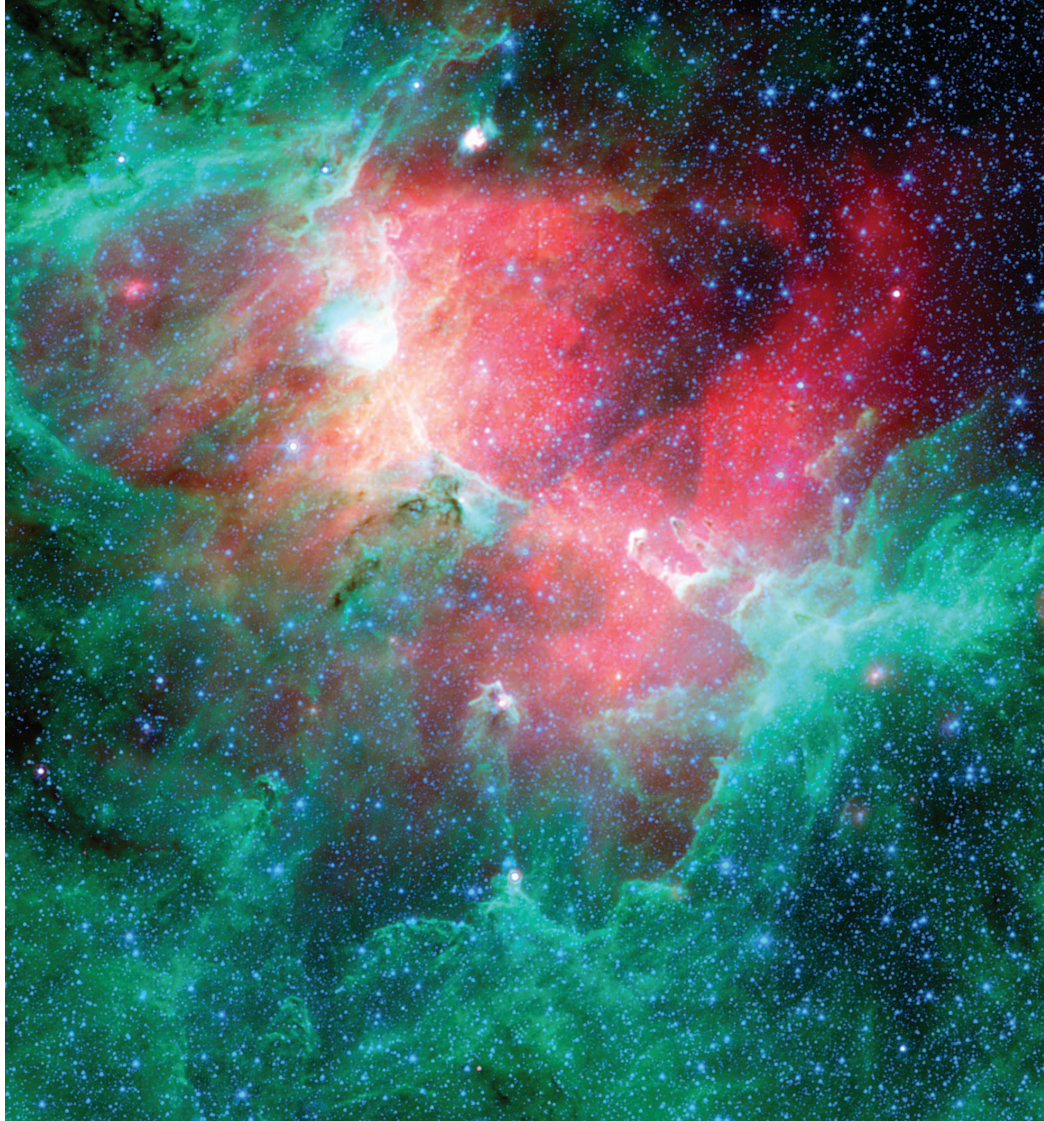


DAVID S. BAYARD,  
BRYAN H. KANG,  
PAUL B. BRUGAROLAS, and  
DHEMETRIOS BOUSSALIS

## AN INTEGRATED HIGH-ORDER KALMAN FILTER APPROACH



INFRARED EAGLE NEBULA (M16), SPITZER SPACE TELESCOPE, IRAC AND MIPS. PHOTO COURTESY OF NASA JPL-CALTECH

# Focal Plane Calibration of the Spitzer Space Telescope

**T**he Spitzer space telescope (Spitzer) is currently NASA's largest and most sensitive infrared (IR) telescope in space. Spitzer generates breakthrough discoveries and fundamental astronomical findings on an almost daily basis and is revolutionizing our understanding of the cosmos [1]. Shown in Figure 1, Spitzer represents the fourth and final element in NASA's Great Observatory program, complementing the range of wavelengths observed by previous program elements comprised of the Hubble space telescope for visual, the Chandra X-ray Observatory for X ray, and the Compton Gamma Ray Obser-

vatory for gamma rays. Spitzer was launched in August 2003 and has operated successfully for over five years.

The Spitzer telescope has an 85-cm aperture and is *diffraction limited* to 6.5  $\mu\text{m}$  (microns), which means that the telescope is designed to achieve the theoretical limit of imaging resolution at this IR wavelength. The instrument uses nonrenewable cryogen to cool the critical optical and detector units. Spitzer's focal plane, shown in Figure 2, carries detectors from three science instruments, namely, the infrared array camera (IRAC), the infrared spectrograph (IRS), and the multiband imaging photometer for Spitzer (MIPS). A list of acronyms is provided in Table 1 to aid discussion. All instrument arrays and spectroscopy apertures

Digital Object Identifier 10.1109/MCS.2009.934466

## Spitzer generates breakthrough discoveries and fundamental astronomical findings on an almost daily basis and is revolutionizing our understanding of the cosmos.

are located in the telescope's circular focal plane, which is cooled to a temperature of 1.5 K. IRAC is designed to provide imaging over wavelengths ranging from 1.8 to 27  $\mu\text{m}$ . IRS, which provides medium-resolution spectra of astrophysical objects over wavelengths ranging from 4 to 200  $\mu\text{m}$ , also includes *peak-up arrays*, which are special detectors in the focal plane that provide real-time centroids of targeted IR objects. These peak-up centroids locate an IR object in the focal plane and facilitate its transfer to the center of narrow spectroscopy slits [2] located elsewhere in the focal plane. MIPS provides imaging and large area mapping over wavelengths ranging from 20 to 200  $\mu\text{m}$ . A main distinguishing element of the MIPS instrument is its scanning mirror, which scans about a single axis in coordination with spacecraft motions to facilitate science observations.

The star tracker, which is a standalone camera mounted on the spacecraft bus, images stars and uses their patterns to determine the tracker's attitude with respect to a specified inertial frame. Since the star tracker attitude is directly measured, the telescope attitude can be determined by establishing its orientation relative to the star tracker.



**FIGURE 1** The Spitzer Space Telescope. Spitzer is NASA's latest infrared telescope and the final element in NASA's Great Observatory program. Spitzer orbits the Sun rather than Earth. This type of orbit is ideal for an infrared telescope because it avoids Earth as a significant source of thermal radiation. Spitzer flies in a 1-AU (astronomical unit) heliocentric Earth-trailing orbit, slowly moving away from Earth with a small drift rate of about 0.1 AU per year. Spitzer has an 85-cm telescope aperture and uses expendable cryogen to cool the critical optical and detector units (courtesy of NASA/JPL-Caltech).

The focal plane includes two pointing control reference sensors (PCRSs) whose primary function is to provide star centroids for maintaining knowledge of the telescope alignment with respect to the star tracker.

Each PCRS is a  $4 \times 4$  pixel array comprised of 10-arcsec pixels, where the four central pixels are calibrated to provide centroids to an accuracy of 1/100th pixel. The PCRSs are redundant with separate A and B units, where the two A-unit PCRSs are baselined for normal operations.

To support a broad range of science instrument requirements and observing modes [3], the Spitzer pointing control system achieves arcsecond-level pointing accuracy and subarcsecond pointing jitter. Before precision pointing is possible, calibration of the telescope focal plane and relevant pointing frames must be performed. This focal-plane calibration procedure is performed during the three-month in-orbit checkout (IOC) period following launch and prior to commissioning. Because the focal plane is cryogenically cooled so that temperatures remain nearly constant throughout the mission, the calibration is performed once and remains valid until mission completion. Cryogen is expended over the mission's life, which is completed when the cryogen is depleted.

Designing a focal-plane calibration procedure for the Spitzer telescope requires overcoming many challenges. These challenges include achieving stringent calibration accuracies on the order of 0.14 arcsec, meeting time-critical

**TABLE 1** Acronyms.

Acronym	Definition
AU	Astronomical unit
CCD	Charge-coupled device
ICRS	International celestial reference system
IOC	In-orbit checkout
IPF	Instrument pointing frame
IR	Infrared
IRAC	Infrared array camera
IRS	Infrared spectrograph
JPL	Jet Propulsion Laboratory
MIPS	Multiband imaging photometer for Spitzer
NASA	National Aeronautics and Space Administration
OAP	Oriented angular pixel
OET	Observatory engineering team
PCRS	Pointing control reference sensor
QR	Orthogonal upper triangular matrix factorization
SED	Spectral energy distribution spectroscopy slit
STA	Star tracker assembly
TPF	Telescope pointing frame

**In this article we discuss the instrument pointing frame (IPF) Kalman filter, which is used to calibrate Spitzer's telescope focal plane.**

operation schedules, and dealing with several science array types, such as imaging cameras, spectroscopy slits, and scanning-type arrays. Being a cryogenically cooled telescope, all Spitzer operations are time critical and are driven by the need to avoid wasting valuable cryogen on nonscience activities.

In this article we discuss the instrument pointing frame (IPF) Kalman filter, which is used to calibrate Spitzer's telescope focal plane [4], [5], [6]. The IPF filter is a high-order square-root iterated linearized Kalman filter that carries 37 states to estimate frame misalignments, while correcting for systematic errors due to optical distortions, scan-mirror errors, thermomechanically induced drift variations, and gyro bias and drift in all axes. Gyro-scale factor and alignment parameters are not included because they are calibrated using a separate dedicated in-flight gyro-calibration filter.

Various Kalman filter approaches to calibrating frame alignments and focal-plane distortions are considered in [7]–[13], while overviews of the sensor alignment literature are given in [9] and [13]. A recent survey of algorithms for calibrating spacecraft attitude sensors and gyros is given in [14].

The IPF Kalman filter generalizes earlier calibration approaches by combining science and engineering parameters into a single high-order filter formulation [5]. On typical missions, these parameters are calibrated separately and often with iterative back-and-forth steps performed by multiple teams of analysts. Aside from being suboptimal and time consuming, analysis in [10] indicates that these iterations may not converge. The integrated IPF Kalman filter method overcomes these limitations and provides convergent estimates with higher accuracy and improved operational efficiency. The Spitzer mission embraces the IPF Kalman filter as its main estimation approach to support all focal-plane survey efforts. Because of its high order, the IPF Kalman filter is designed using special scalings, an array square-root filtering formulation, and measurement strategies that ensure observability of all key parameters.

During the IOC period between September and November 2003, the IPF calibration Kalman filter was applied to 76 data sets to calibrate 128 instrument pointing frames [15]. Altogether, these calibrations represent over 1200 focal-plane parameters characterizing alignments, plate scales, and optical distortions. This article discusses the design of the IPF Kalman filter and its application to calibration data sets, the resulting performance, and the use of the calibration products by the Spitzer mission.

## FOCAL PLANE CALIBRATION

### Performance Requirements

The telescope focal plane is shown projected onto the *celestial sphere* in Figure 2. The celestial sphere is a conceptual sphere of gigantic radius, concentric with the Earth, and onto which all objects in the sky are projected. Figure 2 shows the viewpoint of an observer located inside the celestial sphere. The alignment of each of the 19 *prime frames* is calibrated as part of the focal-plane survey. Each prime frame is calibrated using data from a separate dedicated calibration maneuver. For each prime frame, several neighboring *inferred frames* are calibrated simultaneously using the same data. Spitzer's frame calibration requirements are tabulated in Table 2 for each instrument array. The most stringent survey requirement is 0.14 arcsec, 1- $\sigma$  radial. A 1- $\sigma$  radial requirement of, say  $\alpha$ , indicates that the error is contained in a circle of radius  $\alpha$  to a statistical confidence of 63.21%. For a zero-mean two-dimensional Gaussian error with standard deviation  $\rho$  on each axis, the radius of the 63.21% circle is given by  $\alpha = \sqrt{2}\rho$ , or more simply stated, the factor of  $\sqrt{2}$  converts a 1- $\sigma$  single-axis requirement into a 1- $\sigma$  radial requirement.

**TABLE 2 Instrument pointing frame (IPF) alignment accuracy requirements (arcsec, 1- $\sigma$  radial) for fine focal-plane survey. To accommodate the three-month telescope cool-down schedule, the Spitzer focal-plane surveys are split into three categories, pre-coarse, coarse, and fine. The pre-coarse and coarse focal-plane surveys allow successive refinements of calibration parameters while the telescope is still cooling. The most accurate calibrations are made during the fine surveys, which occur after the telescope is fully cooled and after final telescope focus adjustments have been made. The most stringent survey requirement is 0.14 arcsec, 1- $\sigma$  radial.**

Array/Slit	Required TPF to IPF Alignment	
	Coarse (arcsec)	Fine (arcsec)
IRS peak-up arrays	1	0.25
IRS peak-up sweet spots	1	0.14
IRS short $\lambda$ slits	1	0.14
IRS long $\lambda$ slits	1	0.28
IRAC arrays	1	0.14
MIPS 24- $\mu\text{m}$	1	0.14
MIPS 70- $\mu\text{m}$ fine	1.12	1.1
MIPS 70- $\mu\text{m}$	2.65	2.6
MIPS 160- $\mu\text{m}$	3.75	3.7
MIPS SED	1.15	1.1

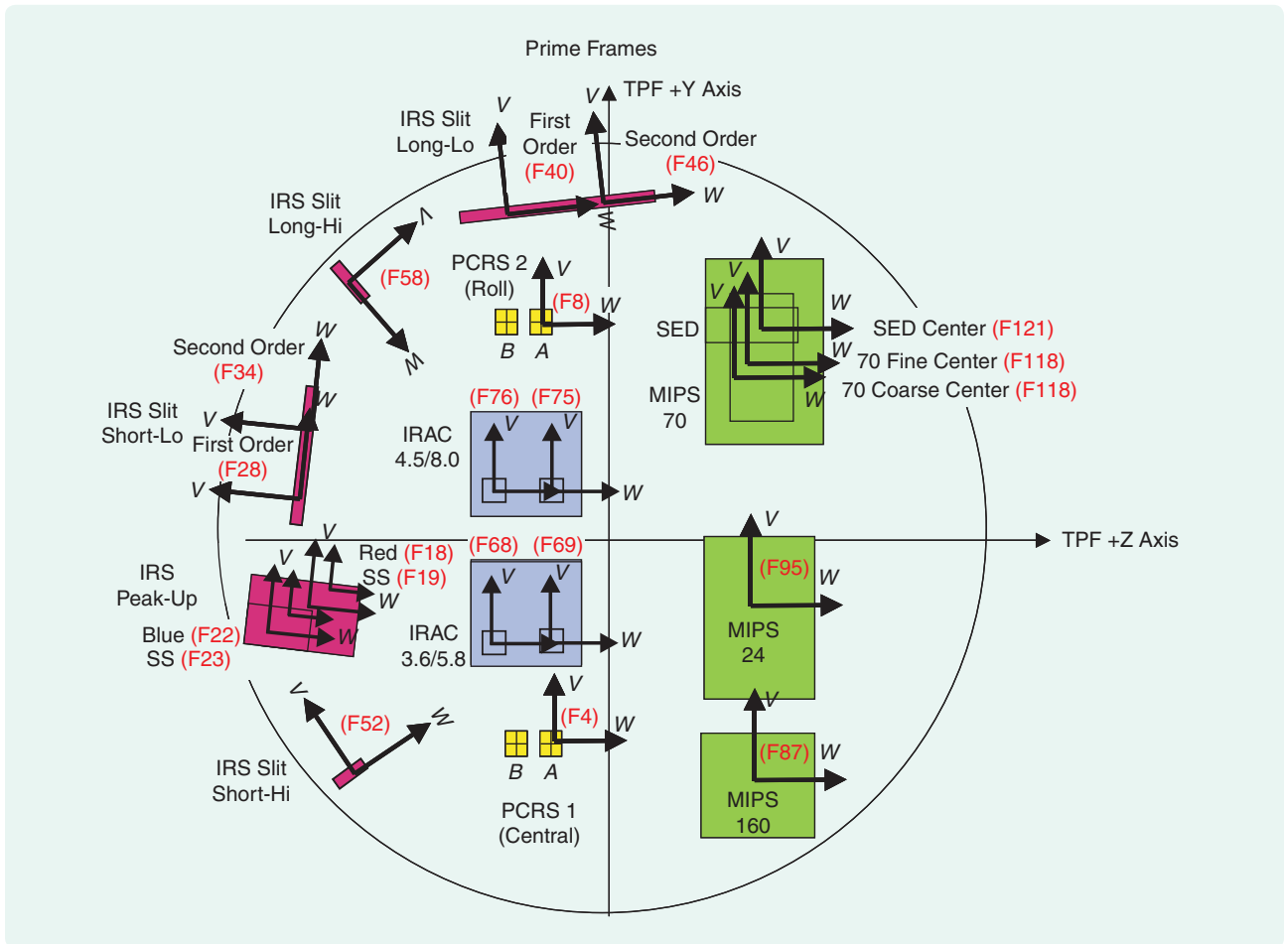


**FIGURE 2** Spitzer's 32-arcmin diameter focal plane showing the infrared array camera, infrared spectrograph, and multiband imaging photometer for Spitzer arrays (not drawn to scale). Each of the 19 prime frames is indicated by two orthogonal axes corresponding to its  $v$ ,  $w$  axes. Also indicated are two pointing control reference sensor frames used for pointing control reference. Each local frame is defined by  $(u, v, w)$  coordinates, where the direction  $u = v \times w$  points toward the celestial sphere. For spectroscopy slits, the direction  $v$  is chosen along the *dispersion direction*, defined by the shorter dimension of a rectangular slit. The focal plane is shown projected onto the celestial sphere, as viewed by an observer located inside the sphere. The telescope pointing frame (TPF)  $x$ -axis defines the telescope boresight that points toward the celestial sphere. During normal operations, the TPF  $z$ -axis is maintained to point in the general direction of the Sun in order to keep sunlight on the solar panels.

### Pointing-Relevant Frames

The sequence of frames and transformations used to parameterize Spitzer's end-to-end pointing chain is shown in Figure 3 and summarized in Table 3. The quantities  $A, R, T, C$  are  $3 \times 3$  direction cosine matrices.

The international celestial reference system (ICRS) frame serves as Spitzer's principal inertial reference frame [16]. The ICRS frame, which is defined in terms of 608 extragalactic radio sources, simplifies and improves on previously used inertial reference frames whose definitions are complicated by Earth wobble, star motion, and parallax.

The star-tracker instrument frame defines Spitzer's body frame with the  $x$ -axis in the boresight direction [6]. The mapping from ICRS to the spacecraft body frame, which is called the *spacecraft attitude*, is described by the direction cosine matrix  $A$ .

During a focal-plane calibration maneuver, only gyro-propagated attitude solutions are used by the IPF filter to estimate attitude. The true attitude matrix  $A(t)$  can be written at each time  $t$  as

$$A(t) = G(t)A_0, \quad (1)$$

where  $G(t)$  is a time-varying  $3 \times 3$  direction cosine matrix, and  $A_0$  is the true initial attitude. In practice, we use an estimate of  $A_0$  defined by the onboard attitude estimate at the initial time, and  $G(t)$  is estimated by propagating a corrected gyro measurement, as explained in the section "Attitude and Gyro Parameters." The telescope pointing frame (TPF), which has the telescope boresight as its  $x$ -axis, is defined in terms of the null points of the two PCRSs [6]. The mapping from the body frame to the TPF is given by the alignment matrix  $R$ .

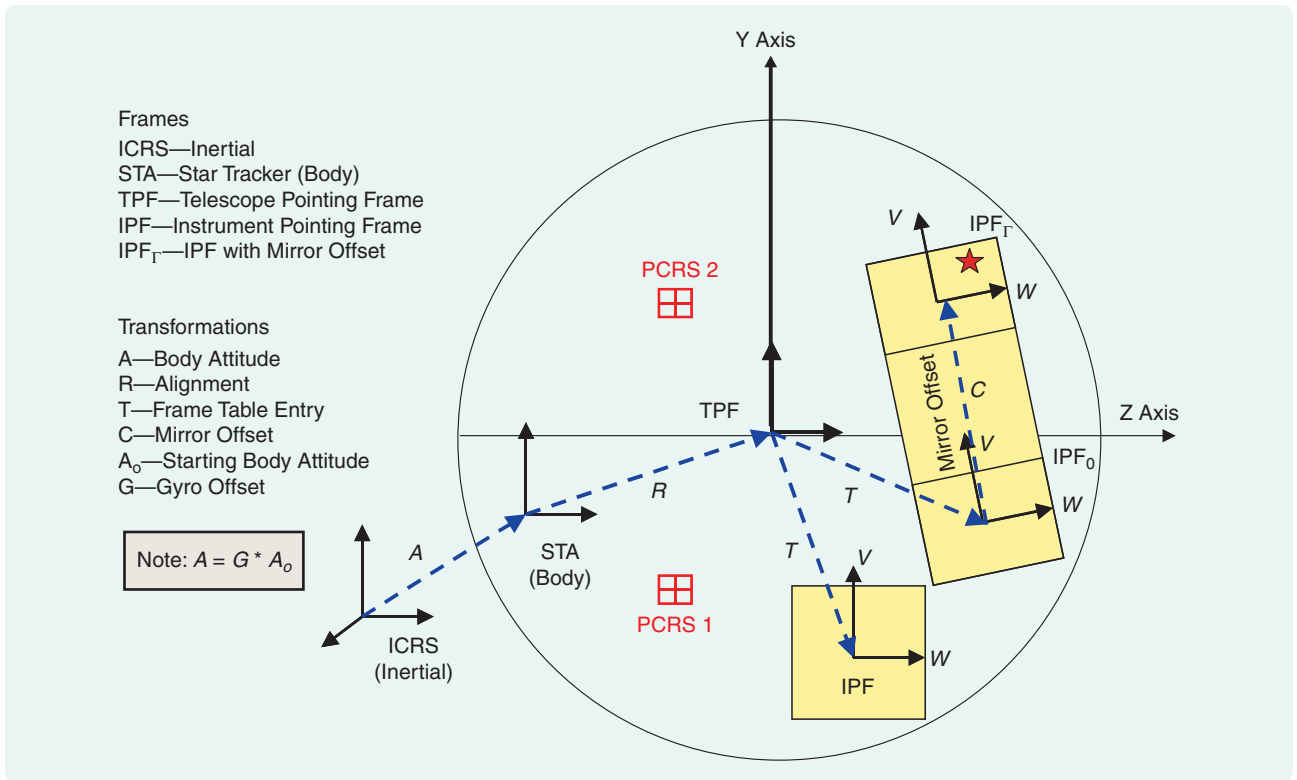


**FIGURE 3** Spitzer frames and transformations. The focal plane is shown projected on the celestial sphere, as it would appear to an observer looking from inside the sphere. The attitude  $A$  is time varying due to intentional telescope repositioning and unintentional control errors. The alignment matrix  $R$  is time varying due to thermomechanically induced alignment drift. The mapping  $T$  from telescope pointing frame to instrument pointing frame is assumed to be constant due to the fact that the telescope focal plane is actively cooled. The mapping  $C$  is time varying due to the constantly changing, but nominally known, scan-mirror offset angle  $\Gamma$ .

The IPF is defined by a pixel location within a specified science array. The IPF coordinate axes are defined by the orientation of a row and column of the pixel array. The mapping from the TPF to any specified IPF is denoted generically by the  $3 \times 3$  matrix  $T$ . The best estimate of each IPF frame is stored in an onboard *frame table* as a quaternion value for  $T$ . The onboard frame table contains all frames that are to be pointed during the five-year mission. For Spitzer, 128 frames are sufficient to cover all of the desired pointing frame options. The frame table is used extensively for attitude commanding during flight operations. Spitzer's prime frames are defined at the center pixel location of each instrument array. For each prime frame, several neighboring inferred frames are defined by their pixel offset relative to the array's prime frame. The nominal orientations of the science instruments and their associated prime frames in the telescope focal plane are shown in Figure 2. Also shown are the mission-accepted conventions for the  $w$  and  $v$  directions, defined for each frame. Specifically, each IPF frame is defined by the  $u, v, w$  coordinate axes, where  $v, w$  are shown in the figure, and  $u = v \times w$  defines a local line-of-sight direction that points toward the celestial sphere. The main goal of the IPF Kalman filter is to accurately estimate the IPF frame  $T$  for each of the 128 prime and inferred frames listed in the onboard frame table.

The direction cosine matrix  $C$  represents a scan-mirror offset from the nominal starting position  $\Gamma = 0$  to its current-local-offset position  $\Gamma \neq 0$ . For non-MIPS instruments, the matrix  $C$  is set to the identity. For MIPS, the frame defined when the scan mirror is offset by the angle  $\Gamma$  is denoted as IPF<sub>Γ</sub>. As the scan mirror moves, an entire family of IPF<sub>Γ</sub> frames is generated as a function of  $\Gamma$ .

The IPF Kalman filter is designed to estimate all frames  $A, R, T, C$  by representing  $T$  as constant,  $A, R$  as polynomial functions of time, and  $C$  as a polynomial function of  $\Gamma$ . The values of  $T$  and parameterized functions  $C(\Gamma)$  are

**TABLE 3** Spitzer pointing chain transformations as  $3 \times 3$  direction cosine matrices  $A, R, T, C$ . The sequence of transformations embodied in the expression  $s = CTRA\ell$  characterizes the end-to-end pointing chain by mapping a unit star location vector  $\ell$  in the ICRS frame to a unit vector  $s$  in the instrument pointing frame IPF<sub>Γ</sub>.

Transformation	Description	From	To
A	Attitude	ICRS	Body
R	Alignment	Body	TPF
T	Instrument	TPF	IPF <sub>0</sub>
C	Scan Mirror Offset	IPF <sub>0</sub>	IPF <sub>Γ</sub>

## Optical distortion parameters capture imperfections and variations in the telescope and instrument that cause a star image location to deviate from its idealized geometric projection.

stored as the main products of the focal-plane survey. These quantities do not change during the mission due to the cryogenically cooled focal plane. The time-varying matrices  $A$  and  $R$  are re-estimated recursively in normal operations and used in conjunction with the stored values of  $T$  and  $C$  to provide an end-to-end description of the Spitzer pointing chain. This pointing chain description supports real-time pointing control as well as after-the-fact pixel-to-sky *pointing reconstruction*. Pointing reconstruction is the process in which astronomical objects of interest seen at specific pixel locations in images are mapped to their corresponding coordinates on the celestial sphere. This information is collected into catalogs and used by the science community to identify IR objects in subsequent studies.

### Sandwich Maneuvers

The calibration of the focal plane is performed using a series of *sandwich maneuvers*. A generic sandwich maneuver, shown in Figure 4, is created from the set of science centroids sandwiched between PCRS measurements. The centroids taken on the science array result in a time-tagged list of  $x$  and  $y$  pixel coordinates for the centroid values. This approach allows for arbitrary grid patterns, dither patterns, or natural star clusters. For the MIPS instrument, the time-tagged list of centroids includes additional information about commanded scan-mirror offsets.

Intuitively, the first measurements on PCRS1 and PCRS2 coupled with the initial star tracker measurement provide information that ensures observability of the telescope alignment matrix  $R$ . The observability of all other calibration parameters is ensured by transitioning between PCRS2, the science array, and then back to PCRS1. Starting and ending the sandwich maneuver on PCRS1 allows the *gyro bias and drift* to be estimated, which in turn corrects for relative attitude propagation during the sandwich maneuver. Gyro bias and drift errors are discussed in the section "Attitude and Gyro Parameters." The sandwich approach uncouples focal-plane-calibration errors from potentially large absolute errors in the initial attitude, which would otherwise degrade overall calibration accuracy.

The sandwich maneuvers are repeated multiple times to ensure that the random errors are sufficiently reduced by the calibration process.

### Standard Coordinates

Let  $u \in \mathcal{R}^3$  be a unit vector associated with a star location in the ICRS frame, where

$$u = \begin{bmatrix} \cos(\text{DEC})\cos(\text{RA}) \\ \cos(\text{DEC})\sin(\text{RA}) \\ \sin(\text{DEC}) \end{bmatrix}, \quad (2)$$

and RA and DEC denote the right ascension and declination of the star. The RA, DEC star locations are obtained from a catalog of stars in ICRS.

Let  $\ell \in \mathcal{R}^3$  denote the unit vector that arises after a velocity aberration correction [17] is applied to  $u$ , where

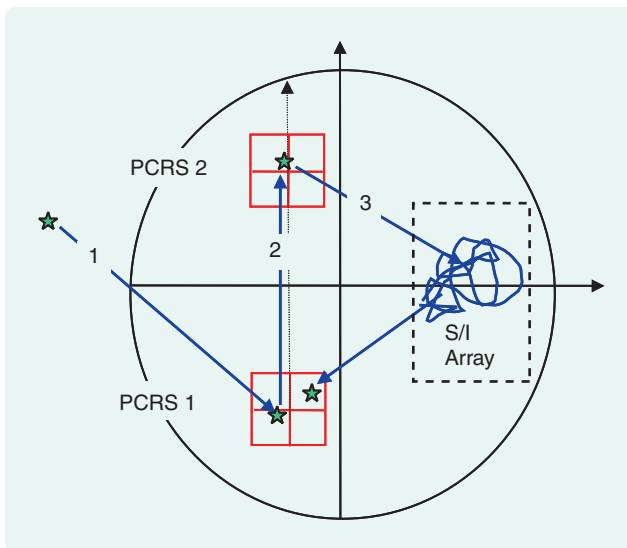


**FIGURE 4** Sandwich maneuver. This maneuver is comprised of the following sequence of steps: 1) locate a target star image on the first pointing control reference sensor (PCRS) detector, PCRS1, and take one or more centroid measurements; 2) move the target star image to PCRS2, and take one or more centroid measurements; 3) move the target star image to several positions on the desired science instrument array, and take a centroid measurement at each location, for example, a 3x3 grid pattern; 4) return to the PCRS1 detector, and take one or more centroid measurements. Starting and ending on PCRS1 calibrates the gyro-propagated relative attitude, which makes calibration results less sensitive to the initial absolute attitude error.

## The IPF Kalman filter is designed as a variable-dimension filter that does not require all parameters to be estimated in all runs.

$$\ell = \frac{u + \frac{1}{c}V_{SC}}{\left\|u + \frac{1}{c}V_{SC}\right\|}, \quad (3)$$

$c$  denotes the speed of light, and  $V_{SC}$  denotes the spacecraft velocity vector relative to the solar-system barycenter.

Define the unit vector  $s \in \mathcal{R}^3$  as the resolution of  $\ell$  in the IPF<sub>T</sub> frame to give

$$s = CTRA\ell, \quad (4)$$

where the  $3 \times 3$  direction cosine matrices  $A, R, T, C$  are defined in Table 3. Substituting (1) into (4) gives

$$s = CTRGA_0\ell. \quad (5)$$

Equation (5) is useful because it shows the complete mapping of a star location vector  $\ell$  in the ICRS frame to a unit vector  $s$  in the desired instrument pointing frame IPF<sub>T</sub>. The next step is to geometrically project  $s$  onto the plane of the science array.

Let the components of  $s$  be given as

$$s = \begin{bmatrix} s_x \\ s_y \\ s_z \end{bmatrix}. \quad (6)$$

Since  $s$  is a unit vector resolved in the IPF<sub>T</sub> frame, it can be projected onto the focal plane to obtain the scaled focal-plane *standard coordinates*

$$z = \begin{bmatrix} z_w \\ z_v \end{bmatrix} = \begin{bmatrix} s_z/s_x \\ s_y/s_x \end{bmatrix}. \quad (7)$$

The Spitzer focal plane is parameterized in terms of the sets  $p_1$  and  $p_{2f}$  of parameters, which are summarized in Table 4 and Table 5, respectively. Roughly speaking,  $p_1$  contains *science* parameters while  $p_{2f}$  contains *engineering* parameters in the sense that  $p_1$  calibrates science camera image distortions, while  $p_{2f}$  calibrates key frame alignments and gyro behaviors. Incremental forms of  $p_1$  and  $p_{2f}$ , which are included in the tables as  $\delta p_1$  and  $\delta p_2$ , respectively, are used for linearization purposes. The parameters  $p_1$  are

unconstrained so that both  $p_1$  and  $\delta p_1$  are of dimension 17. In contrast, the subscript “ $f$ ” in  $p_{2f}$  emphasizes that it has the full 24 parameters, whereas its incremental form  $\delta p_2$  has only 20 parameters. This difference is due to four constraints that enter into the problem, where  $\delta p_2$  captures only the unconstrained degrees of freedom. Two of the constraints are due to quaternions  $q_T$  and  $q_R$  that are unit-normalized as  $\|q_T\| = 1$ ,  $\|q_R\| = 1$ , and two constraints are due to the scan-mirror axis orientation vector  $a_m = [a_{m1}, a_{m2}, a_{m3}]$ , which is unit-normalized as  $\|a_m\| = 1$  and is constrained to allow only in-plane rotations  $a_{m1} = 0$ . The IPF Kalman filter has  $37 = 20 + 17$  states since it is linearized and carries only states for the incremental parameters  $\delta p_1$  and  $\delta p_2$ . Calibration parameters are discussed in more detail in subsequent sections.

Let the matrices  $C, T, R, G$  be parameterized in terms of the components of  $p_{2f}$ , and let the initial attitude  $A_0$  be related to an available initial attitude estimate  $\hat{A}_0$  by means of

$$A_0 = (I - \psi^\times)\hat{A}_0, \quad (8)$$

where  $\psi = [\psi_x, \psi_y, \psi_z]^T \in \mathcal{R}^3$  is a small-angle rotation vector that parameterizes the initial attitude error, and the matrix cross-product notation is defined by

**TABLE 4 Science calibration parameters  $p_1$ , perturbation vector  $\delta p_1$ , and mask vector mask1. The vector  $p_1$  has 17 parameters associated with the size and distorted shape of the science camera pixels as projected outward onto the celestial sphere. The incremental vector  $\delta p_1$  is used for linearization. The mask1 vector is a 17-element binary vector that indicates which parameters  $\delta p_1$  are included in the variable-dimension IPF Kalman filter.**

$p_1$	Math	Description	$\delta p_1$	Mask
$p_1(1)$	$a_{00}$	Constant plate scales	$\delta p_1(1)$	mask1(1)
$p_1(2)$	$b_{00}$		$\delta p_1(2)$	mask1(2)
$p_1(3)$	$c_{00}$	$\Gamma$ -dependent plate scales	$\delta p_1(3)$	mask1(3)
$p_1(4)$	$a_{10}$		$\delta p_1(4)$	mask1(4)
$p_1(5)$	$b_{10}$		$\delta p_1(5)$	mask1(5)
$p_1(6)$	$c_{10}$		$\delta p_1(6)$	mask1(6)
$p_1(7)$	$d_{10}$		$\delta p_1(7)$	mask1(7)
$p_1(8)$	$a_{20}$	$\Gamma^2$ -dependent plate scales	$\delta p_1(8)$	mask1(8)
$p_1(9)$	$b_{20}$		$\delta p_1(9)$	mask1(9)
$p_1(10)$	$c_{20}$		$\delta p_1(10)$	mask1(10)
$p_1(11)$	$d_{20}$	Linear plate scales	$\delta p_1(11)$	mask1(11)
$p_1(12)$	$a_{01}$		$\delta p_1(12)$	mask1(12)
$p_1(13)$	$b_{01}$		$\delta p_1(13)$	mask1(13)
$p_1(14)$	$c_{01}$		$\delta p_1(14)$	mask1(14)
$p_1(15)$	$d_{01}$		$\delta p_1(15)$	mask1(15)
$p_1(16)$	$e_{01}$		$\delta p_1(16)$	mask1(16)
$p_1(17)$	$f_{01}$		$\delta p_1(17)$	mask1(17)

## The a posteriori joint covariance matrix from the integrated Kalman filter is indispensable for preflight design of calibration experiments.

$$\psi^\times \triangleq \begin{bmatrix} 0 & -\psi_z & \psi_y \\ \psi_z & 0 & -\psi_x \\ -\psi_y & \psi_x & 0 \end{bmatrix}. \quad (9)$$

The vector  $\psi$  is treated as measurement error. We can write (7) in the functional form

$$z = h_z(p_{2f}, \psi). \quad (10)$$

This representation of the target-source location in standard coordinates is the starting point for the calibration process.

### Oriented Angular Pixel (OAP) Coordinates

Science centroid locations are conveniently specified in units of pixels in a local  $x, y$  coordinate system defined over the detector. For example, if the detector is a charge-coupled device (CCD), the  $x$  and  $y$  axes are often defined

along the pixel row and column directions of the detector. However, calibration is more easily performed if pixel measurements are converted to angular units in radians and expressed with respect to a specified origin and orientation. Oriented angular pixel (OAP) coordinates serve this purpose.

A pixel coordinate  $(c_x, c_y)$  in the instrument  $(x, y)$  coordinate system is converted to OAP coordinates using the transformation

$$y = \begin{bmatrix} y_w \\ y_v \end{bmatrix} = D \begin{bmatrix} \rho_x & 0 \\ 0 & \rho_y \end{bmatrix} \begin{bmatrix} c_x - c_{x0} \\ c_y - c_{y0} \end{bmatrix}, \quad (11)$$

$$D \triangleq \begin{bmatrix} d_{11} & d_{12} \\ d_{21} & d_{22} \end{bmatrix}. \quad (12)$$

Here,  $\rho_x$  and  $\rho_y$  are nominal plate scales, which relate the angular size of an object in space projected onto the celestial sphere, to its linear size on the detector, and the pixel

**TABLE 5 Engineering calibration parameters  $p_{2f}$ , perturbation vector  $\delta p_2$ , and mask vector mask2. The vector  $p_{2f}$  has 24 parameters, which include scan-mirror misalignments, frame alignments  $T$  and  $R$ , linear and quadratic drifts in  $R$ , and gyro bias and drift. The incremental form  $\delta p_2$  is used for linearization and has only 20 parameters due to four physical constraints that are enforced. The mask2 vector is a 20-element binary vector, which indicates the components of  $\delta p_2$  that are included in the variable-dimension IPF Kalman filter.**

$p_{2f}$	Math	Description	$\delta p_2$	Mask
$p_{2f}(1)$	$a_{m1}$	Mirror rotation axis unit vector in IPF (x)		
$p_{2f}(2)$	$a_{m2}$	Mirror rotation axis unit vector in IPF (y)	$\delta\alpha$	mask2(1)
$p_{2f}(3)$	$a_{m3}$	Mirror rotation axis unit vector in IPF (z)		
$p_{2f}(4)$	$\beta$	Scan mirror rotation angle scale factor	$\delta\beta$	mask2(2)
$p_{2f}(5)$	$q_{T1}$	T (TPF to IPF) frame quaternion, $q_T(1)$	$\delta\theta_1$	mask2(3)
$p_{2f}(6)$	$q_{T2}$	T (TPF to IPF) frame quaternion, $q_T(2)$	$\delta\theta_2$	mask2(4)
$p_{2f}(7)$	$q_{T3}$	T (TPF to IPF) frame quaternion, $q_T(3)$	$\delta\theta_3$	mask2(5)
$p_{2f}(8)$	$q_{T4}$	T (TPF to IPF) frame quaternion, $q_T(4)$		
$p_{2f}(9)$	$q_{R1}$	R alignment quaternion, $q_R(1)$	$\delta a_{rx}$	mask2(6)
$p_{2f}(10)$	$q_{R2}$	R alignment quaternion, $q_R(2)$	$\delta a_{ry}$	mask2(7)
$p_{2f}(11)$	$q_{R3}$	R alignment quaternion, $q_R(3)$	$\delta a_{rz}$	mask2(8)
$p_{2f}(12)$	$q_{R4}$	R alignment quaternion, $q_R(4)$		
$p_{2f}(13)$	$b_{rx}$	Linear time-varying contribution on alignment x-axis	$\delta b_{rx}$	mask2(9)
$p_{2f}(14)$	$b_{ry}$	Linear time-varying contribution on alignment y-axis	$\delta b_{ry}$	mask2(10)
$p_{2f}(15)$	$b_{rz}$	Linear time-varying contribution on alignment z-axis	$\delta b_{rz}$	mask2(11)
$p_{2f}(16)$	$c_{rx}$	Quadratic time-varying contribution on alignment x-axis	$\delta c_{rx}$	mask2(12)
$p_{2f}(17)$	$c_{ry}$	Quadratic time-varying contribution on alignment y-axis	$\delta c_{ry}$	mask2(13)
$p_{2f}(18)$	$c_{rz}$	Quadratic time-varying contribution on alignment z-axis	$\delta c_{rz}$	mask2(14)
$p_{2f}(19)$	$b_{gx}$	Gyro bias, x-axis	$\delta b_{gx}$	mask2(15)
$p_{2f}(20)$	$b_{gy}$	Gyro bias, y-axis	$\delta b_{gy}$	mask2(16)
$p_{2f}(21)$	$b_{gz}$	Gyro bias, z-axis	$\delta b_{gz}$	mask2(17)
$p_{2f}(22)$	$c_{gx}$	Gyro bias drift, x-axis	$\delta c_{gx}$	mask2(18)
$p_{2f}(23)$	$c_{gy}$	Gyro bias drift, y-axis	$\delta c_{gy}$	mask2(19)
$p_{2f}(24)$	$c_{gz}$	Gyro bias drift, z-axis	$\delta c_{gz}$	mask2(20)

coordinate  $(c_{x0}, c_{y0})$  specifies the desired location where the prime frame is to be embedded.

The quantities  $d_{11}, d_{12}, d_{21}, d_{22}$ , which are flip parameters taking on possible values 0, -1, +1, specify the polarities associated with how the instrument coordinate directions  $(x, y)$  map into the focal plane coordinate directions  $(w, v)$  defined in Figure 2.

### Mapping OAP Coordinates to Standard Coordinates

Let  $y_{\text{true}} \in \mathcal{R}^2$  be a target source as observed in OAP coordinates assuming the centroiding error is zero and with the components

$$y_{\text{true}} = \begin{bmatrix} y_{w,\text{true}} \\ y_{v,\text{true}} \end{bmatrix}. \quad (13)$$

Generally,  $y_{\text{true}}$  does not coincide exactly with  $z$  in (10) due to imperfections in the optical system. To accommodate these imperfections, a model mapping  $y_{\text{true}}$  in OAP coordinates to  $z$  in standard coordinates is taken to be of the form

$$z = \begin{bmatrix} z_w \\ z_v \end{bmatrix} = (I + M(p_1, \Gamma, y_{\text{true}})) \begin{bmatrix} y_{w,\text{true}} \\ y_{v,\text{true}} \end{bmatrix}, \quad (14)$$

where the perturbation matrix  $M \in \mathcal{R}^{2 \times 2}$  captures imperfections such as optical distortions and plate-scale errors. The exact form of  $M$  is discussed below as a function of  $p_1$ , the scan mirror offset angle  $\Gamma$ , and the centroid location  $y_{\text{true}}$ .

Relation (14) assumes noiseless centroids. To generalize the model, a noisy centroid  $y$  is used to replace  $y_{\text{true}}$  in (14) according to the relation

$$z = \begin{bmatrix} z_w \\ z_v \end{bmatrix} = (I + M(p_1, \Gamma, y)) \begin{bmatrix} y_w \\ y_v \end{bmatrix} - \nu, \quad (15)$$

where  $\nu$  denotes the centroiding error in  $y$ . The motivation for choosing this model is that, for  $M = 0$ , (15) simplifies to the additive noise model  $y \approx y_{\text{true}} + \nu$ .

### Calibration Equation

Equating (10) and (15) yields the calibration equation

$$(I + M(p_1, \Gamma, y))y = h_z(p_{2f}, \psi) + \nu, \quad (16)$$

which is the main relationship used for all Spitzer's focal-plane calibration. The calibration equation (16) is an end-to-end relation in the sense that it maps the source location on the celestial sphere, which is known from a star catalog with velocity aberration correction applied, to the pixel location at which source is observed on the science instrument array. The calibration equation (16) is parameterized by science parameters  $p_1$  and engineering parameters  $p_{2f}$ .

The parameters  $p_1$  and  $p_{2f}$  are treated as constant and unknown, whereas the sensor noise  $\nu$  and attitude error  $\psi$  are treated as measurement noise with specific correlation patterns. Specifically,  $\nu$  is taken as independent from centroid to centroid, while  $\psi$  is taken as independent from sandwich maneuver to sandwich maneuver. The end-to-end

pointing transformations associated with the calibration equation (16) are summarized in Figure 5.

## IPF FILTER PARAMETERS

### Full-State Description

The starting point for the Kalman filter design is the calibration equation (16). The full-state vector  $x_f$  is defined as

$$x_f = \begin{bmatrix} p_1 \\ p_{2f} \end{bmatrix}, \quad (17)$$

where  $p_1$  are the 17 science parameters and  $p_{2f}$  are the 24 engineering parameters in the calibration equation (16).

### Scan-Mirror Rotation Parameters

Mathematically, the scan-mirror offset matrix  $C$  is parameterized as the eigenaxis rotation

$$C(p_{2f}, \Gamma) = \cos(\beta\Gamma)I + (1 - \cos(\beta\Gamma))a_m a_m^T - \sin(\beta\Gamma)a_m^\times, \quad (18)$$

where  $a_m = [a_{m1}, a_{m2}, a_{m3}]^T$  is the scan-mirror spin axis,  $\Gamma$  is the measured scan-mirror angle in radians, and  $\beta$  is the scale factor associated with the measured mirror angle. As a scale factor,  $\beta$  captures errors in the along-scan direction. The vector  $a_m$  is constrained to have unit norm and is further constrained to lie in the local plane of the celestial sphere, which corresponds to  $a_{m1} = 0$ . These two constraints leave one degree of freedom, denoted by  $\alpha$ , which captures errors in the cross-scan direction. Scan-mirror errors are calibrated by  $\alpha$  and  $\beta$ , which together capture errors in the cross-scan and along-scan directions.

The mirror transformation becomes the identity when the mirror is located in its nominal reference position  $\Gamma = 0$ , that is,

$$C(p_{2f}, 0) = I. \quad (19)$$

The condition  $C = I$  is enforced for non-MIPS instruments since they do not have a scan mirror.

### Optical Distortion Parameters

Optical distortion parameters capture imperfections and variations in the telescope and instrument that cause a star image location to deviate from its idealized geometric projection. The optical distortions in the calibration equation (16) are parameterized in terms of the matrix  $M \in \mathcal{R}^{2 \times 2}$  by means of

$$M(p_1, \Gamma, y) = M_{00} + \Gamma M_{10} + \Gamma^2 M_{20} + M_{01}(y), \quad (20)$$

$$\begin{aligned} M_{00} &= \begin{bmatrix} a_{00} & c_{00} \\ c_{00} & b_{00} \end{bmatrix}, & M_{10} &= \begin{bmatrix} a_{10} & c_{10} \\ d_{10} & b_{10} \end{bmatrix}, \\ M_{20} &= \begin{bmatrix} a_{20} & c_{20} \\ d_{20} & b_{20} \end{bmatrix}, \end{aligned} \quad (21)$$

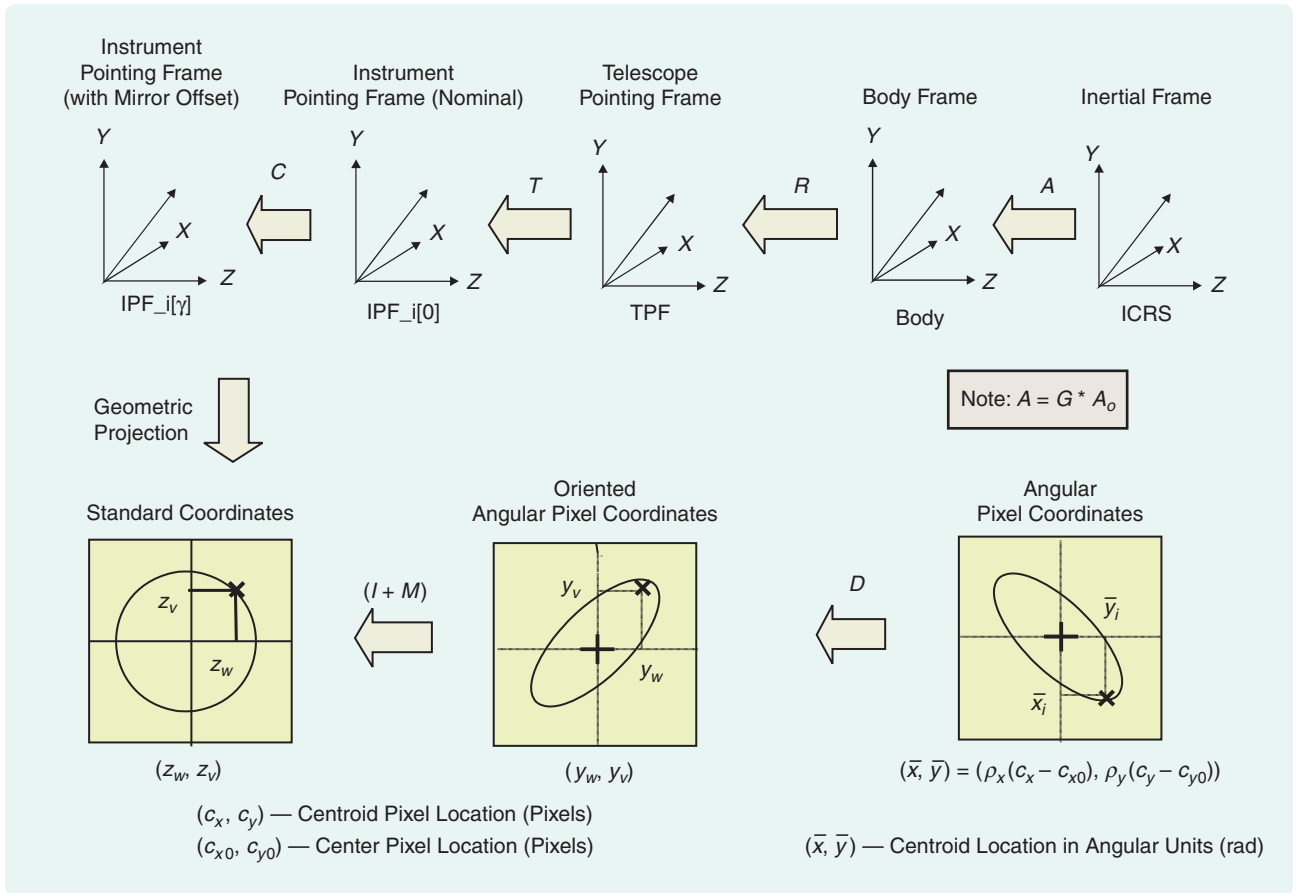


**FIGURE 5** End-to-end pointing transformations. This sequence of transformations indicates how the pixel locations  $(c_x, c_y)$  map into unit vectors in the international celestial reference system frame. For calibration purposes it is convenient to meet halfway in this diagram and bring all quantities to standard coordinates. In particular, equating all relevant quantities in standard coordinates yields the calibration equation (16), which serves as the main measurement equation for filtering purposes.

$$M_{01}(y) = \begin{bmatrix} a_{01}y_w + c_{01}y_v & b_{01}y_v \\ d_{01}y_w & f_{01}y_w + e_{01}y_v \end{bmatrix}. \quad (22)$$

Care is taken in specifying optical distortion parameters so that they are not redundant with engineering parameters. Specifically, consider a non-MIPS array by letting  $\Gamma = 0$  in (20). The analysis in [10] indicates that two offset terms and one rotational term must be eliminated from the optical distortion parameterization to avoid redundancy with the three rotations associated with the alignment matrix  $T$ . The two offset terms are eliminated by omitting them from the optical distortion parameterization (20), and the rotational term is eliminated by repeating the parameter  $c_{00}$  symmetrically in (21) to ensure that the  $2 \times 2$  matrix  $M_{00}$  has no skew-symmetric component.

### Telescope Frame Parameters

The alignment matrix  $T$ , which transforms from TPF to  $IPF_0$ , is represented by a quaternion  $q_T = [q_{T1}, q_{T2}, q_{T3}, q_{T4}]^T$  according to (23), shown at the bottom of the page. Given an estimate  $\hat{T}$ , the matrix  $T$  is linearized as

$$T = (I - \delta\theta^\times) \hat{T}, \quad (24)$$

where  $\delta\theta = [\delta\theta_1, \delta\theta_2, \delta\theta_3]^T$ .

### Thermomechanical Drift Parameters

The direction cosine matrix  $R$  represents the time-varying mapping from the STA-defined body frame to the TPF frame. The mapping varies primarily due to thermomechanically induced boresight shifts over time. Starting at

$$T(q_T) = \begin{bmatrix} q_{T1}^2 - q_{T2}^2 - q_{T3}^2 + q_{T4}^2 & 2(q_{T1}q_{T2} + q_{T3}q_{T4}) & 2(q_{T1}q_{T3} - q_{T2}q_{T4}) \\ 2(q_{T1}q_{T2} - q_{T3}q_{T4}) & q_{T2}^2 - q_{T3}^2 + q_{T4}^2 - q_{T1}^2 & 2(q_{T2}q_{T3} + q_{T1}q_{T4}) \\ 2(q_{T1}q_{T3} + q_{T2}q_{T4}) & 2(q_{T2}q_{T3} - q_{T1}q_{T4}) & q_{T3}^2 + q_{T4}^2 - q_{T1}^2 - q_{T2}^2 \end{bmatrix}. \quad (23)$$

**TABLE 6 Example instrument pointing frame (IPF) filter execution mask-vector assignment for the multiband imaging photometer for Spitzer (MIPS) 24- $\mu\text{m}$  array. Mask vectors indicate, by unity elements, which calibration parameters to use in the variable-dimension IPF Kalman filter. MIPS arrays typically need the most parameters since they have additional scan-mirror parameters, while the infrared spectrograph spectroscopy slits need the fewest parameters to characterize the size and shape of the entrance aperture.**

Const. Plate			$\Gamma$	$\Gamma^2$	Lin. Plate	Mirror		IPF (T)			Alignment R		Gyro
$a_{00}$	$b_{00}$	$c_{00}$	$a_{10} \dots d_{10}$	$a_{20} \dots d_{20}$	$a_{01} \dots f_{01}$	$\alpha$	$\beta$	$\theta_1$	$\theta_2$	$\theta_3$	$a_r$	$b_r, c_r$	$b_g, c_g$
1	2	3	4-7	8-11	12-17	1	2	3	4	5	6-8	9-14	15-20
1	1	1	1	0	1	1	1	1	1	1	1	1	1

the initial alignment  $R_0(q_R)$ , the IPF filter parameterizes  $R$  as the quadratic function of time given by

$$R \triangleq \left( I_{3 \times 3} - \left( b_r t + c_r \frac{t^2}{2} \right)^\times \right) R_0(q_R), \quad (25)$$

where

$$b_r = \begin{bmatrix} b_{rx} \\ b_{ry} \\ b_{rz} \end{bmatrix}, \quad c_r = \begin{bmatrix} c_{rx} \\ c_{ry} \\ c_{rz} \end{bmatrix}. \quad (26)$$

The time  $t = 0$  in (25) corresponds to the time tag of the first centroid of the first sandwich maneuver. The quantity  $R_0$  represents the STA-to-TPF alignment at  $t = 0$ , which is initialized by an estimate from a separate onboard filter [3]. For notational simplicity, the quaternion equivalent of the initial alignment  $R_0$  is denoted as  $q_R$  rather than  $q_{R0}$ . Given the estimate  $\hat{R}_0$ , the matrix  $R_0$  is linearized as

$$R_0 = (I - \delta a^\times) \hat{R}_0, \quad (27)$$

where  $\delta a = [\delta a_{rx}, \delta a_{ry}, \delta a_{rz}]^T$ .

### Attitude and Gyro Parameters

The offset attitude  $G(t)$  defined in (1) propagates by integrating the true rate  $\omega \in \mathcal{R}^3$  as

$$\dot{G} = -\omega^\times G. \quad (28)$$

Since the true rate  $\omega \in \mathcal{R}^3$  is not known, an estimate must be generated. For convenience, this computation is done in two stages.

First, the gyro preprocessor calculates a nominal rate vector estimate  $\omega_m^\circ \in \mathcal{R}^3$  by subtracting, from the raw gyro measurement, a coarse estimate of the gyro bias available from the onboard pointing system [6]. In practice,  $\omega_m^\circ$  will be close to the true rate  $\omega$  but not perfect.

Second, the time-varying correction  $b_g + c_g t$  is added to the nominal rate vector  $\omega_m^\circ$  to model the true rate  $\omega$  in the form

$$\omega = \omega_m^\circ + b_g + c_g t. \quad (29)$$

The term  $b_g \in \mathcal{R}^3$ , entering as a constant rate error, is the *gyro bias*, whereas the term  $c_g \in \mathcal{R}^3$ , entering as a linearly growing rate error, is the *gyro drift*. This equation represents a truth model for the physical rate  $\omega$ . Since the correc-

tion parameters  $b_g$  and  $c_g$  are not known, they are estimated by  $\hat{b}_g$  and  $\hat{c}_g$  as part of the Kalman filter state, leading to the estimated rate in the form

$$\hat{\omega} = \omega_m^\circ + \hat{b}_g + \hat{c}_g t. \quad (30)$$

This two-stage approach allows the gyro sensitivity equations to be computed once and stored, rather than requiring complete repropagation during every filter cycle, thus speeding up the Kalman filter computation. This method assumes that the nominal rate  $\omega_m^\circ$  is sufficiently close to the true rate  $\omega$  to allow linearization of the estimation problem for all future iterations. If this assumption is false, an option to repropagate the sensitivities is provided.

### IPF Parameter Mask

The IPF Kalman filter is designed as a variable-dimension filter that does not require all parameters to be estimated in all runs. Parameters to be retained in a particular run are specified by unity elements in an associated binary mask vector. The illustrative binary mask shown as the last row of Table 6 is used to calibrate the MIPS 24- $\mu\text{m}$  array. Mask vectors used in all of the fine calibration surveys are summarized in Table 7 and Table 8.

The number of calibration parameters is adjusted based on various factors, such as array type, required accuracy, and the quality of the calibration data. Precoarse and coarse surveys are typically calibrated using fewer parameters than fine surveys since precoarse and coarse surveys contain fewer sandwich maneuvers, are less informative, and are performed during the first two months of the mission while the telescope is still cooling.

## FILTER MECHANIZATION

### IPF Kalman Filter Architecture

The IPF Kalman filter algorithm is architected as a square-root iterated linearized Kalman filter. The filter operates in block sequential form as summarized in Figure 6. Each time the forward path of Figure 6 is completed, a parameter correction is applied, the filter is re-linearized, and the forward path is recomputed. This process defines an iterative Kalman filter implementation. As an example, Figure 7 shows correction size as a function of the iteration number for a typical MIPS 24- $\mu\text{m}$  array calibration run. Corrections for this

**TABLE 7** Final mask vector assignment for  $\delta p_1$  calibration parameters. The infrared spectrograph IRS, infrared array camera (IRAC) and multiband imaging photometer for Spitzer (MIPS) camera arrays (frames 18–23, 68–76, 95–118), calibrate all three constant plate scales  $a_{00}$ ,  $b_{00}$ ,  $c_{00}$ , while the IRS (28–58) and MIPS SED (121) spectroscopy slits calibrate the scale factor  $a_{00}$  in only the cross-dispersion direction. The MIPS 160- $\mu\text{m}$  array (87) contains only 2 rows of pixels, and is treated as a spectroscopy slit for calibration purposes. The  $\Gamma$ -dependent terms  $a_{10}$ ,  $b_{10}$ ,  $c_{10}$ ,  $d_{10}$  are useful for calibrating the MIPS arrays, which optically distort as a polynomial function of the scan mirror offset  $\Gamma$ . The  $\Gamma^2$ -dependent terms, also available to the IPF filter, are not needed to obtain accurate results in the fine surveys. The linear plate scales are useful for calibrating large-format arrays operating at short wavelengths (IRS 18,22, IRAC 68–76, MIPS 95).

Parameter Description		Const. Plate			$\Gamma$	$\Gamma^2$	Lin. Plate
$p_1$ Parameters		$a_{00}$	$b_{00}$	$c_{00}$	$a_{10} \dots d_{10}$	$a_{20} \dots d_{20}$	$a_{01} \dots f_{01}$
Instrument Name	NF	1	2	3	4–7	8–11	12–17
IRS Red PeakUp: center of FOV	18	1	1	1	0	0	1
IRS Red PeakUp: sweet spot	19	1	1	1	0	0	0
IRS Blue PeakUp: center of FOV	22	1	1	1	0	0	1
IRS Blue PeakUp: sweet spot	23	1	1	1	0	0	0
IRS ShortLo Slit: first-order center	28	1	0	0	0	0	0
IRS ShortLo Slit: second-order center	34	1	0	0	0	0	0
IRS LongLo Slit: first-order center	40	1	0	0	0	0	0
IRS LongLo Slit: second-order center	46	1	0	0	0	0	0
IRS ShortHi Slit: center	52	1	0	0	0	0	0
IRS LongHi Slit: center	58	1	0	0	0	0	0
IRAC center of 3.6- $\mu\text{m}$ array	68	1	1	1	0	0	1
IRAC center of 5.8- $\mu\text{m}$ array	69	1	1	1	0	0	1
IRAC center of 4.5- $\mu\text{m}$ array	75	1	1	1	0	0	1
IRAC center of 8.0- $\mu\text{m}$ array	76	1	1	1	0	0	1
MIPS center of 160- $\mu\text{m}$ array	87	0	0	0	0	0	0
MIPS center of 24- $\mu\text{m}$ array	95	1	1	1	1	0	1
MIPS center of 70- $\mu\text{m}$ array	107	1	1	1	0	0	0
MIPS center of 70- $\mu\text{m}$ fine array	118	1	1	1	0	0	0
MIPS center of SED	121	0	0	0	0	0	0

**TABLE 8** Final mask-vector assignment for calibration parameters  $\delta p_2$ . Scan-mirror misalignments  $\alpha$ ,  $\beta$  are relevant only to the multiband imaging photometer for Spitzer (MIPS) arrays. The instrument pointing frame alignment parameters  $\theta_1$ ,  $\theta_2$ ,  $\theta_3$  are estimated for all frames, except for the spectroscopy slits, which use preflight values of  $\theta_1$  to prescribe their orientation angle on the sky. The star tracker assembly to pointing control reference sensor (STA-to-PCRS) alignment matrix  $R$  is estimated as a quadratic function of time for all arrays except for infrared array camera IRAC arrays, which estimates a constant  $R$  due to short duration maneuvers. The MIPS 160- $\mu\text{m}$  array (frame 87) is calibrated with the fewest parameters due to its simple two-pixel-row geometry, and less stringent calibration requirements. Gyro drift is removed as a quadratic function of time in all calibrations except for the MIPS 160- $\mu\text{m}$  array.

Parameter Description		Mirror		IPF (T)			Alignment R		Gyro
$p_2$ Parameters		$\alpha$	$\beta$	$\theta_1$	$\theta_2$	$\theta_3$	$a_r$	$b_r, c_r$	$b_g, c_g$
Instrument Name	NF	1	2	3	4	5	6–8	9–14	15–20
IRS Red PeakUp: center of FOV	18	0	0	1	1	1	1	1	1
IRS Red PeakUp: sweet spot	19	0	0	1	1	1	1	1	1
IRS Blue PeakUp: center of FOV	22	0	0	1	1	1	1	1	1
IRS Blue PeakUp: sweet spot	23	0	0	1	1	1	1	1	1
IRS ShortLo Slit: first-order center	28	0	0	0	1	1	1	1	1
IRS ShortLo Slit: second-order center	34	0	0	0	1	1	1	1	1
IRS LongLo Slit: first-order center	40	0	0	0	1	1	1	1	1
IRS LongLo Slit: second-order center	46	0	0	0	1	1	1	1	1
IRS ShortHi Slit: center	52	0	0	0	1	1	1	1	1
IRS LongHi Slit: center	58	0	0	0	1	1	1	1	1
IRAC center of 3.6- $\mu\text{m}$ array	68	0	0	1	1	1	1	0	1
IRAC center of 5.8- $\mu\text{m}$ array	69	0	0	1	1	1	1	0	1
IRAC center of 4.5- $\mu\text{m}$ array	75	0	0	1	1	1	1	0	1
IRAC center of 8.0- $\mu\text{m}$ array	76	0	0	1	1	1	1	0	1
MIPS center of 160- $\mu\text{m}$ array	87	1	0	1	1	1	0	0	0
MIPS center of 24- $\mu\text{m}$ array	95	1	1	1	1	1	1	1	1
MIPS center of 70- $\mu\text{m}$ array	107	1	1	1	1	1	1	1	1
MIPS center of 70- $\mu\text{m}$ fine array	118	1	1	1	1	1	1	1	1
MIPS center of SED	121	1	1	1	1	1	1	1	1

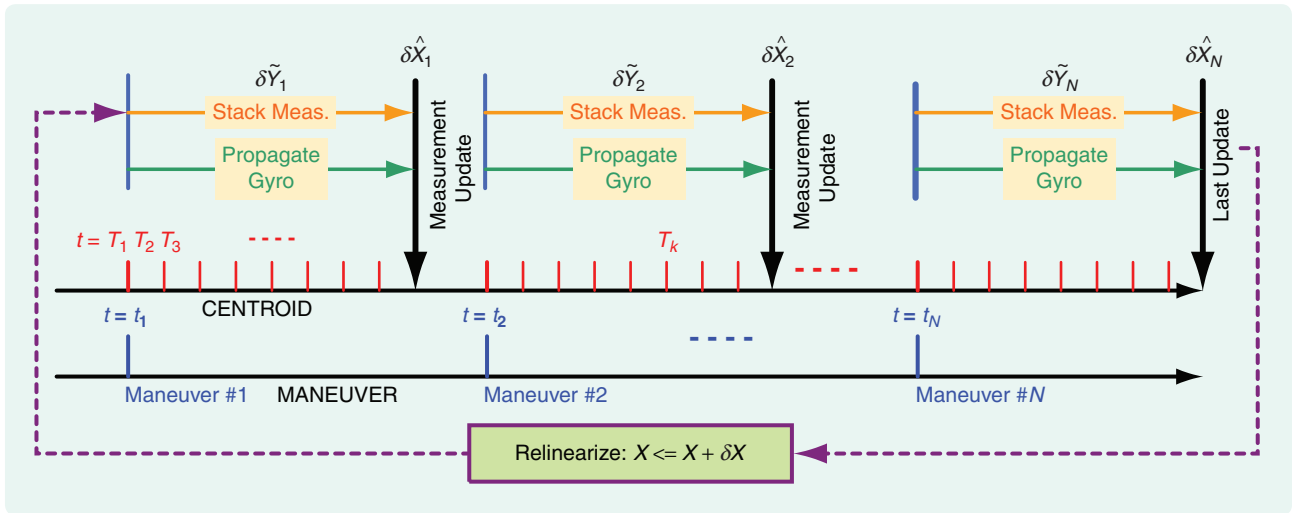


**FIGURE 6** Square-root, iterated, and linearized Kalman filtering process. First, a nominal state estimate used for linearization purposes is prescribed at the beginning of the data set corresponding to  $t = 0$ . The start time of the  $j$ th sandwich maneuver is  $t_j$ , and the individual centroid times are  $T_k$ . Centroid data from each sandwich maneuver are “stacked” into a tall measurement vector, which is used to update the Kalman filter. Accordingly, for a calibration data set having  $N$  sandwich maneuvers, there are  $N$  vector measurement updates. After processing the entire data set, the estimated state correction is applied, and the filter is relinearized about the updated state estimate. This process of relinearization is repeated until convergence is obtained.

example converge in about ten iterations, and most calibration runs converge in less than 20 iterations.

### Linearization with Constraints

As mentioned above, the perturbation  $\delta p_2 \in \mathcal{R}^{20}$  has a smaller dimension than the vector  $p_{2f} \in \mathcal{R}^{24}$  that it perturbs. This property is due to constraints that exist in the problem. In general, the derivative of a function  $f(\xi_f) \in \mathcal{R}^n$  with respect to a constrained parameter vector  $\xi_f \in \mathcal{R}^m$  is defined in terms of only the independent parameters  $\delta \xi \in \mathcal{R}^m$ , where  $m \leq m_f$  by the matrix  $\mathcal{K} \in \mathcal{R}^{n \times m}$  that satisfies

$$f(\xi_f) = f(\hat{\xi}_f) + \mathcal{K}\delta\xi + \mathcal{O}(\|\delta\xi\|^2). \quad (31)$$

This derivative is written as

$$\mathcal{K} \triangleq \left. \frac{\partial f}{\partial(\delta\xi)} \right|_{\xi_f = \hat{\xi}_f}, \quad (32)$$

where the columns of  $\mathcal{K}$  are directional derivatives in the unconstrained basis directions of the tangent plane to the constraint manifold. In this sense, notation (32) represents a slight abuse of notation since it is not a full derivative but rather a derivative of the function  $f$  with respect to a generally lower order unconstrained set of variables. However, the meaning of this notation should be clear from the context. As an example, consider the function  $f(A) = Ax$  where  $A$  is constrained to be an orthogonal matrix,  $\hat{A}$  is a known approximation to  $A$ , and  $x$  is a prescribed vector. Then for  $\hat{A}$  sufficiently close to  $A$ , the perturbation vector  $\delta a \in \mathcal{R}^3$  can be defined such that

$$f(A) = Ax = (I - \delta a^\times) \hat{A}x + \mathcal{O}(\|\delta a\|^2), \quad (33)$$

$$= \hat{A}x + (\hat{A}x)^\times \delta a + \mathcal{O}(\|\delta a\|^2). \quad (34)$$

Equation (34) is exactly in the form of (31) with  $f(\hat{A}) = \hat{A}x$  and  $\mathcal{K} = (\hat{A}x)^\times$ .

### Time Propagation Equation

Corresponding to the full-state vector  $x_f$  defined in (17), a state-vector perturbation is given as

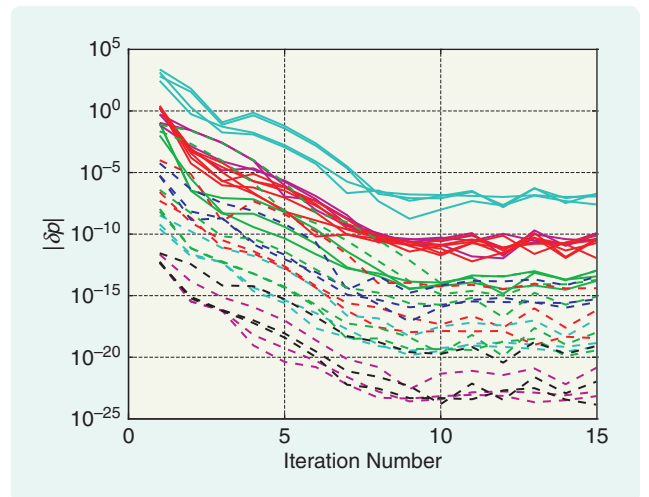


**FIGURE 7** Iterated Kalman filter correction size as a function of iteration number. Parameter correction magnitudes are shown for the science parameters  $\delta p_1$  (solid), and the engineering parameters  $\delta p_2$  (dash), associated with a typical multiband imaging photometer for a Spitzer 24- $\mu\text{m}$  calibration run. Convergence is obtained in approximately ten iterations, after which the correction size no longer decreases systematically.

## The integrated calibration approach enables powerful data pruning methods to be developed based on a posteriori filter residuals.

$$\delta x = \begin{bmatrix} \delta p_1 \\ \delta p_2 \end{bmatrix} \in \mathcal{R}^{37}, \quad (35)$$

where  $\delta p_1 \in \mathcal{R}^{17}$  and  $\delta p_2 \in \mathcal{R}^{20}$ .

Since the IPF Kalman filter is parameterized by constant coefficients, the state perturbation propagation equation can be written as

$$\delta \dot{x} = \begin{bmatrix} \dot{\delta p}_1 \\ \dot{\delta p}_2 \end{bmatrix} = 0. \quad (36)$$

The final IPF filter implementation uses a constant parameter assumption (36), aided by a covariance reset at the start of each new campaign to better accommodate possible large and discontinuous parameter changes. Propagating an iterative Kalman filter without process noise is equivalent to solving the underlying minimum-variance nonlinear least-squares problem using a Gauss-Newton algorithm [18].

The discrete form of the state-perturbation propagation equations for the mean and square-root covariance can be written as

$$\delta \hat{x}_{j+1|j} = \delta \hat{x}_{j|j}, \quad (37)$$

$$P_{j+1|j}^{\text{ch}} = P_{j|j}^{\text{ch}}, \quad (38)$$

where  $j+1|j$  signifies the predicted value at the start of maneuver  $j+1$ , given measurements from the past  $j$  maneuvers, and  $P^{\text{ch}}$  denotes the lower triangular factor of the positive-definite covariance matrix  $P$  in the Cholesky factorization  $P = P^{\text{ch}} P^{\text{ch}T}$ . Using superscript  $\text{ch}$  for the lower triangular Cholesky factor distinguishes it from  $1/2$  used for the symmetric matrix factor in other applications.

### Measurement Equation

Calibration equation (16) serves as a measurement equation for the Kalman filter. This equation is first rearranged into the form

$$y = h(p_1, p_2, \psi, y) + \nu, \quad (39)$$

where

$$h(p_1, p_2, \psi, y) = -M(p_1, y)y + h_z(p_2, \psi). \quad (40)$$

The measurement  $y$ , which appears on both sides of (39), requires a slight deviation from Kalman filter conventions. This structure arises from the implicit form of  $y$  appearing in (16). Also, the dependence of  $M$  on  $\Gamma$  is dropped here for notational convenience. Interestingly, in the case of slits, the complete measurement  $y$  is not available in any single measurement to evaluate the right-hand side of (40). In this case, the linearization is handled differently, as described in [6].

Equation (39) can be linearized to obtain the desired Kalman filter update equation. Using the nominal state estimates  $\hat{p}_1$  and  $\hat{p}_{2f}$ , a prediction  $\hat{h}$  of  $h$  is constructed of the form

$$\hat{h} = h(\hat{p}_1, \hat{p}_{2f}, 0, y). \quad (41)$$

Subtracting (41) from (39) gives the desired measurement perturbation equation

$$\begin{aligned} \delta y &\triangleq y - h(\hat{p}_1, \hat{p}_{2f}, 0, y) \\ &= \mathcal{K}_1 \delta p_1 + \mathcal{K}_2 \delta p_2 + H_\psi \psi + \nu \\ &= [\mathcal{K}_1 \ \mathcal{K}_2] \begin{bmatrix} \delta p_1 \\ \delta p_2 \end{bmatrix} + H_\psi \psi + \nu \\ &= H \delta x + n, \end{aligned} \quad (42)$$

where

$$H \triangleq [\mathcal{K}_1 \ \mathcal{K}_2],$$

$$\mathcal{K}_1 \triangleq \left. \frac{\partial h}{\partial p_1} \right|_{\hat{p}_1, \hat{p}_{2f}} = \left. \frac{\partial}{\partial p_1} (-M(p_1, y)y) \right|_{\hat{p}_1, \hat{p}_{2f}}, \quad (43)$$

$$\mathcal{K}_2 \triangleq \left. \frac{\partial h_z}{\partial (\delta p_2)} \right|_{\hat{p}_1, \hat{p}_{2f}}, \quad (44)$$

$$H_\psi \triangleq \left. \frac{\partial h_z}{\partial \psi} \right|_{\hat{p}_1, \hat{p}_{2f}}, \quad (45)$$

$$n \triangleq H_\psi \psi + \nu. \quad (46)$$

Equation (42) is the desired measurement-perturbation relation.

Equation (46) describes how the initial attitude error  $\psi$  at the start of a specific maneuver couples into subsequent measurements. The resulting structure for the noise covariance  $\text{cov}(n)$  ensures that the initial attitude error is correctly weighted with respect to the optimal filter. Of course this argument applies to random attitude errors from

maneuver to maneuver. Any systematic component of attitude error common to the initial attitude of all sandwich maneuvers is absorbed into the estimate of  $R$  since the filter does not carry attitude states. This misappropriation of attitude information is not a question of optimality, but rather observability, since a systematic attitude error is physically indistinguishable from an error in the alignment  $R$ . By design, this effect is localized to  $R$ , and has minimal impact on the other calibration parameters, whose accuracies depend almost completely on relative attitude information obtained through gyro propagation.

### Stacked Measurements

Equation (42) provides the measurement perturbation  $\delta y$  associated with a single centroid measurement. For filtering purposes, all of the centroids associated with the  $j$ th maneuver are stacked into the single measurement vector

$$\delta \tilde{y}_j = \tilde{H}_j \delta x + \tilde{n}_j, \quad (47)$$

where

$$\delta \tilde{y}_j \triangleq \begin{bmatrix} \delta y_1 \\ \vdots \\ \delta y_{m_j} \end{bmatrix}, \quad \tilde{n}_j \triangleq \begin{bmatrix} n_1 \\ \vdots \\ n_{m_j} \end{bmatrix}, \quad \tilde{H}_j \triangleq \begin{bmatrix} H_1 \\ \vdots \\ H_{m_j} \end{bmatrix}, \quad (48)$$

and  $m_j$  is the number of centroids in the  $j$ th maneuver.

Because of the special structure of the noise  $n$  in (46), the stacked noise term  $\tilde{n}_j$  in (47) can be broken down into two separate terms as

$$\tilde{n}_j = \tilde{v}_j + \tilde{H}_{\psi,j} \psi_j, \quad (49)$$

where

$$\tilde{v}_j \triangleq \begin{bmatrix} v_1 \\ \vdots \\ v_{m_j} \end{bmatrix}, \quad \tilde{H}_{\psi,j} \triangleq \begin{bmatrix} H_{\psi,1} \\ \vdots \\ H_{\psi,m_j} \end{bmatrix}. \quad (50)$$

In (49) we use the fact that the initial attitude error  $\psi_j \in \mathcal{R}^3$  associated with the  $j$ th maneuver contributes to all of the measurements  $\delta \tilde{y}_j \in \mathcal{R}^{2m_j}$  taken during that maneuver.

Assuming independence of centroiding and attitude errors, the covariance of  $\tilde{n}_j$  in (49) can be computed as

$$\tilde{R}_j \triangleq \text{cov}(\tilde{n}_j) = \tilde{V}_j + \tilde{H}_{\psi,j} P_{\psi,j} \tilde{H}_{\psi,j}^T, \quad (51)$$

where

$$\tilde{V}_j \triangleq \text{cov}(\tilde{v}_j) = \begin{bmatrix} V_1 & \dots & 0 \\ \vdots & \ddots & \vdots \\ 0 & \dots & V_{m_j} \end{bmatrix}, \quad (52)$$

$$V_i \triangleq \text{cov}(v_i), \quad (53)$$

$$P_{\psi,j} \triangleq \text{cov}(\psi_j). \quad (54)$$

Since numerical conditioning of the Kalman filter is improved by working with square-root covariances [19], define the Cholesky factorizations

$$\tilde{R}_j \triangleq \tilde{R}_j^{\text{ch}} \tilde{R}_j^{\text{ch}T}, \quad (55)$$

$$\tilde{V}_j \triangleq \tilde{V}_j^{\text{ch}} \tilde{V}_j^{\text{ch}T}, \quad (56)$$

$$P_{\psi,j} \triangleq P_{\psi,j}^{\text{ch}} P_{\psi,j}^{\text{ch}T}, \quad (57)$$

where  $X^{\text{ch}T}$  denotes  $X^{\text{ch}}$  transposed for any matrix  $X$ . Using (55)–(57), (51) can be written equivalently as

$$\tilde{R}_j^{\text{ch}} \tilde{R}_j^{\text{ch}T} = \tilde{H}_{\psi,j} P_{\psi,j}^{\text{ch}} P_{\psi,j}^{\text{ch}T} \tilde{H}_{\psi,j}^T + \tilde{V}_j^{\text{ch}} \tilde{V}_j^{\text{ch}T}. \quad (58)$$

Recognizing that (58) has the form  $CC^T = AA^T + BB^T$  with the choices  $A = \tilde{H}_{\psi,j} P_{\psi,j}^{\text{ch}}$  and  $B = \tilde{V}_j^{\text{ch}}$ , the square-root factor  $C = \tilde{R}_j^{\text{ch}}$  is determined as the transpose of the upper triangular factor in the QR factorization of  $[A, B]^T$  [6].

### Measurement Update

Using the stacked measurement equation (47), the Kalman filter gain and square-root covariance update is obtained. Specifically, given  $\tilde{H}_j$ ,  $P_{\psi,j}^{\text{ch}}$ , and  $\tilde{R}_j^{\text{ch}}$ , we consider the unitary triangularization of the matrix

$$\begin{bmatrix} \tilde{R}_j^{\text{ch}} & \tilde{H}_j P_{\psi,j}^{\text{ch}} \\ 0 & P_{\psi,j}^{\text{ch}} \end{bmatrix} = \begin{bmatrix} X & 0 \\ Y & Z \end{bmatrix} \Theta, \quad (59)$$

where  $\Theta$  is an orthogonal matrix. The factorization in (59) is performed using a QR factorization. Extracting  $X$ ,  $Y$ , and  $Z$ , we compute the Kalman filter gain  $K$  and update equation as [19]

$$K_j = YX^{-1}, \quad (60)$$

$$P_{\psi,j}^{\text{ch}} = Z. \quad (61)$$

Given the Kalman gain in (60), the state-perturbation update equation is

$$\delta \hat{x}_{j|j} = \delta \hat{x}_{j|j-1} + K_j (\delta \tilde{y}_j - \tilde{H}_j \delta \hat{x}_{j|j-1}). \quad (62)$$

### Sensitivity Equations Parameters $\delta p_1$

The sensitivity  $\mathcal{K}_1$  is defined from (43) as

$$\mathcal{K}_1 = \frac{\partial}{\partial p_1} (-M(p_1, y)y) \Big|_{\hat{p}_1, \hat{p}_y}. \quad (63)$$

Using Kronecker identities, we can write

$$\begin{aligned} -M(p_1, y)y &= -(M_{00} + \Gamma M_{10} + \Gamma^2 M_{20} + M_{01}(y))y \\ &= -(y^T \otimes I) \text{vec}(M) \\ &= -(y^T \otimes I) [S_{00} \quad \Gamma S_{10} \quad \Gamma^2 S_{20} \quad f_u(y)] p_1, \end{aligned} \quad (64)$$

where

$$S_{00} = \begin{bmatrix} 1 & 0 & 0 \\ 0 & 0 & 1 \\ 0 & 0 & 1 \\ 0 & 1 & 0 \end{bmatrix}, \quad S_{10} = \begin{bmatrix} 1 & 0 & 0 & 0 \\ 0 & 0 & 0 & 1 \\ 0 & 0 & 1 & 0 \\ 0 & 1 & 0 & 0 \end{bmatrix},$$

$$S_{20} = \begin{bmatrix} 1 & 0 & 0 & 0 \\ 0 & 0 & 0 & 1 \\ 0 & 0 & 1 & 0 \\ 0 & 1 & 0 & 0 \end{bmatrix}, \quad (65)$$

$$f_u(y) = \begin{bmatrix} y_w & 0 & y_v & 0 & 0 & 0 \\ 0 & 0 & 0 & y_w & 0 & 0 \\ 0 & y_v & 0 & 0 & 0 & 0 \\ 0 & 0 & 0 & 0 & y_v & y_w \end{bmatrix}, \quad (66)$$

$$y^T \otimes I = \begin{bmatrix} y_w & 0 & y_v & 0 \\ 0 & y_w & 0 & y_v \end{bmatrix}. \quad (67)$$

Substituting (64) into (63) gives the desired expression

$$\mathcal{K}_1 = -(y^T \otimes I)[S_{00} \quad \Gamma S_{10} \quad \Gamma^2 S_{20} \quad f_u(y)]. \quad (68)$$

### Sensitivity Equations for the Parameters $\delta p_2$ and $\psi$

We now compute the sensitivities taken with respect to  $\delta p_2$  and  $\psi$  to define  $\mathcal{K}_2$  and  $H_\psi$  in (44) and (45), respectively. The main idea is to use (5)–(7).

Assume that current estimates  $\hat{C}, \hat{T}, \hat{R}, \hat{G}, \hat{A}_0$  are sufficiently close to  $C, T, R, G, A_0$  so that the small-angle rotation vectors  $c_k, \theta_k, \varphi_k, g_k, \psi_k$  can be defined according to the relationships

$$C = (I - c_k^\times) \hat{C}, \quad (69)$$

$$T = (I - \theta_k^\times) \hat{T}, \quad (70)$$

$$R = (I - \varphi_k^\times) \hat{R}, \quad (71)$$

$$G = (I - g_k^\times) \hat{G}, \quad (72)$$

$$A_0 = (I - \psi_k^\times) \hat{A}_0. \quad (73)$$

Substituting (69)–(73) into (5) and rearranging gives

$$s \triangleq CTRGA_0 \ell \quad (74)$$

$$= (I - c_k^\times) \hat{C} (I - \theta_k^\times) \hat{T} (I - \varphi_k^\times) \hat{R} (I - g_k^\times) \quad (75)$$

$$\times \hat{G} (I - \psi_k^\times) \hat{A}_0 \ell$$

$$= [I - (c_k + \hat{C}\theta_k + \hat{C}\hat{T}\varphi_k + \hat{C}\hat{T}\hat{R}g_k + \hat{C}\hat{T}\hat{R}\hat{G}\psi_k)^\times] \quad (76)$$

$$\times \hat{C}\hat{T}\hat{R}\hat{G}\hat{A}_0 \ell$$

$$= (I - \eta^\times) \hat{N} \ell, \quad (77)$$

where  $\eta$  is the total pointing perturbation given by

$$\eta = c_k + \hat{C}\theta_k + \hat{C}\hat{T}\varphi_k + \hat{C}\hat{T}\hat{R}g_k + \hat{C}\hat{T}\hat{R}\hat{G}\psi_k, \quad (78)$$

and  $\hat{N}$  is the matrix

$$\hat{N} = \hat{C}\hat{T}\hat{R}\hat{G}\hat{A}_0. \quad (79)$$

It is seen from (78) that  $\eta$  can be written as a linear function of the individual perturbations as

$$\eta = [I \quad \hat{C} \quad \hat{C}\hat{T} \quad \hat{C}\hat{T}\hat{R}] \begin{bmatrix} c_k \\ \theta_k \\ \varphi_k \\ g_k \end{bmatrix} + \hat{C}\hat{T}\hat{R}\hat{G}\psi_k \quad (80)$$

$$= H_\eta \lambda_k + L_\psi \psi_k,$$

where

$$\lambda \triangleq [c_k^T \quad \theta_k^T \quad \varphi_k^T \quad g_k^T]^T \in \mathcal{R}^{12},$$

$$H_\eta \triangleq [I \quad \hat{C} \quad \hat{C}\hat{T} \quad \hat{C}\hat{T}\hat{R}],$$

$$L_\psi \triangleq \hat{C}\hat{T}\hat{R}\hat{G}.$$

Given the above construction, the desired sensitivities can be written in the form

$$\mathcal{K}_2 = \frac{\partial h_z}{\partial(\delta p_2)} = \frac{\partial z}{\partial s} \frac{\partial s}{\partial \eta} \frac{\partial \eta}{\partial \lambda} \frac{\partial \lambda}{\partial(\delta p_2)} = H_z H_s H_\eta H_\lambda, \quad (81)$$

$$H_\psi = \frac{\partial h_z}{\partial \psi} = \frac{\partial z}{\partial s} \frac{\partial s}{\partial \eta} \frac{\partial \eta}{\partial \psi} = H_z H_s L_\psi, \quad (82)$$

where the derivatives are evaluated at  $p_1 = \hat{p}_1$ ,  $p_{2f} = \hat{p}_{2f}$ , and  $\psi = 0$ .

## FOCAL PLANE SURVEY RESULTS

Prior knowledge about the Spitzer telescope focal plane is available from optical performance tests performed on the ground in the Brutus chamber at Ball Aerospace and summarized in [20] and [21]. These tests provide the a priori frame alignment information needed to initialize the IPF Kalman filter.

In total, the IPF Kalman filter is used to process 76 separate calibration data sets. These data sets consist of 19 pre-coarse survey runs, 29 coarse survey runs, and 28 fine survey runs. Based on these runs, over 1200 calibration parameters associated with frame alignments, pointing systematic errors, plate scales, and optical distortions are estimated. Complete focal plane survey results are reported in [15]. The fine survey results, which by design are the most accurate, are briefly discussed below.

Fine focal-plane survey results are summarized in Table 9. The choice of calibration parameters estimated for each array are specified by the 0-1 mask vectors shown in Table 7 for  $\delta p_1$ , and in Table 8 for  $\delta p_2$ . The results in Table 9 indicate that all calibration requirements are met with margins ranging from 4% for the IRS Long-Lo slit (frame 046), which has a tight 0.28-arcsec requirement, to 89% for the MIPS 70- $\mu\text{m}$  array

**TABLE 9 Results of Spitzer fine focal-plane survey instrument pointing frame (IPF) alignment accuracy (arcsec, 1- $\sigma$  radial) using the IPF Kalman filter. Radial 1- $\sigma$  pointing error denotes the root-sum-square of the 1- $\sigma$  angular errors from each of the two orthogonal pointing axes. The 1- $\sigma$  angular error for each axis is computed based on the square root of the corresponding diagonal of the Kalman filter covariance matrix, after being scaled by a function of the sum-of-squares a posteriori filter residuals using a method borrowed from linear-regression theory [23]. Comparison with Table 2 indicates that all requirements are met.**

NF	RN	Description	Total (arcsec)	REQ (arcsec)
018	701	IRS Red Peak-up: center of FOV	0.0899	0.25
019	701	IRS Red Peak-up: sweet spot	0.0866	0.14
022	701	IRS Blue Peak-up: center of FOV	0.0966	0.25
023	701	IRS Blue Peak-up: sweet spot	0.0869	0.14
028	502	IRS ShortLo slit: first-order center	0.1165	0.14
034	502	IRS ShortLo slit: second-order center	0.0909	0.14
040	502	IRS LongLo slit: first-order center	0.1295	0.28
046	501	IRS LongLo slit: second-order center	0.2682	0.28
052	502	IRS ShortHi slit: center	0.0885	0.14
058	501	IRS LongHi slit: center	0.1027	0.28
068	502	IRAC center of 3.6- $\mu$ m array	0.0881	0.14
069	502	IRAC center of 5.8- $\mu$ m array	0.0889	0.14
075	502	IRAC center of 4.5- $\mu$ m array	0.0878	0.14
076	502	IRAC center of 8.0- $\mu$ m array	0.0895	0.14
087	703	MIPS center of 160- $\mu$ m array	1.2056	3.70
095	602	MIPS center of 24- $\mu$ m array	0.0884	0.14
107	704	MIPS center of 70- $\mu$ m array	0.2847	2.60
118	702	MIPS center of 70- $\mu$ m fine array	0.3038	1.10
121	703	MIPS center of SED	0.9998	1.10

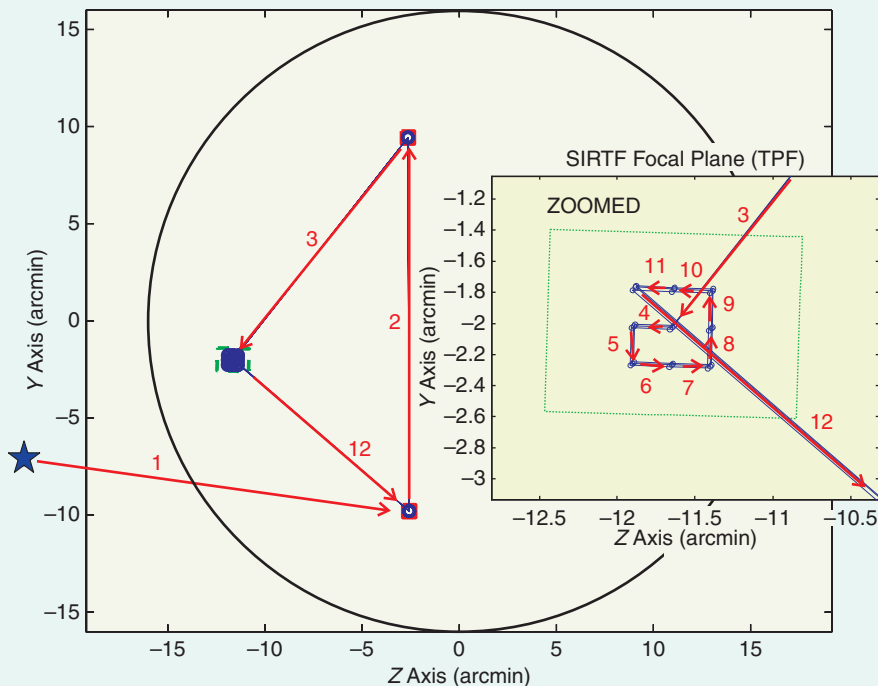


**FIGURE 8** Sandwich maneuver for calibrating the infrared spectrograph red peak-up array. The maneuver places a star image on PCRS1 (leg 1), moves the image to PCRS2 (leg 2), moves the image to the peak-up array (leg 3), where it is placed at each point on a 3  $\times$  3 grid (legs 4–11 shown in zoomed insert), and then moves the star image back to PCRS1 (leg 12). Spacecraft attitude maneuvers are used to move the star image from location to location in the telescope focal plane.

(frame 107), which has a more generous 2.6-arcsec requirement. The worst-case margin of 4% agrees well with pre-flight predictions of 3% [22]. For pointing purposes, the

most critical calibrations are for the IRS peak-up array sweet spots and short wavelength slit centers (frames 019, 023, 052, 028, 034). The results in Table 9 show that these

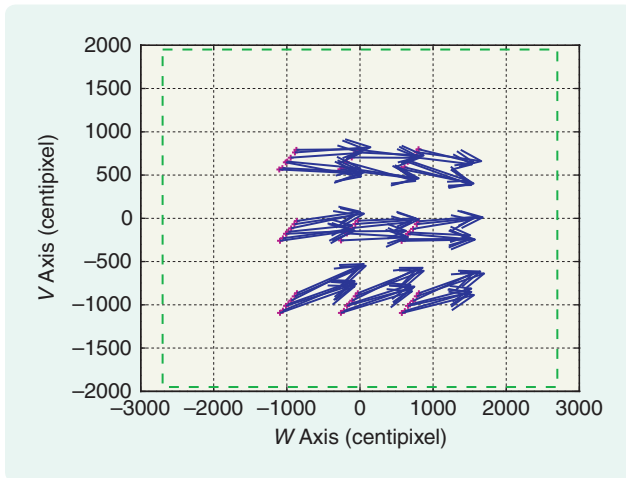


**FIGURE 9** Infrared spectrograph red peak-up array (frame 018) a priori prediction error quiver plot in oriented angular pixel coordinates (centipixels). Quivers point from the prior prediction to the corresponding centroid measurement and are magnified by a factor of ten. Pixels are multiplied by 100 to give units of centipixels, with an angular scale of 0.018 arcsec per centipixel. Long quivers in the same direction indicate a predominant systematic error. The dashed outer box indicates the nominal array size of  $1 \times 1.2$  arcmin as projected onto the celestial sphere.

frames are meeting their 0.14-arcsec requirements with an expected accuracy of approximately 0.09 arcsec, corresponding to a 36% margin.

## CASE STUDIES

### Case Study 1: IRS Red Peak-Up Array (Frame 018)

The IRS peak-up array is calibrated based on the sandwich maneuver shown in Figure 8. The sandwich maneuver is repeated seven times, and consists of a total of 61 science centroids and 49 PCRS measurements. The IPF filter estimates 27 parameters including three constant and six linear plate scales. The pixel size is nominally 1.8 arcsec as projected onto the celestial sphere, equivalent to .018 arcsec per *centipixel*, where a centipixel is defined as 1/100 of a pixel.

A priori prediction errors are plotted as quivers in Figure 9, and a posteriori prediction errors are plotted as quivers in Figure 10. Calibration results indicate that corrections made to the constant plate scale parameters are on the order of 24 parts per thousand. The optical distortion quiver plot in Figure 11 indicates the presence of high-order distortions. Estimation results indicate that the IRS peak-up array achieves a centroiding accuracy on the order of five centipixels, or about 1/20 of a 1.8-arcsec pixel. The frame calibration is accurate to 0.09 arcsec, satisfying its fine survey requirement of 0.25 arcsec by a margin of 28%.

### Case Study 2: IRS Short-Lo Slit (Frame 028)

The IRS short-lo slit is calibrated based on the sandwich maneuver shown in Figure 12. This maneuver is repeated

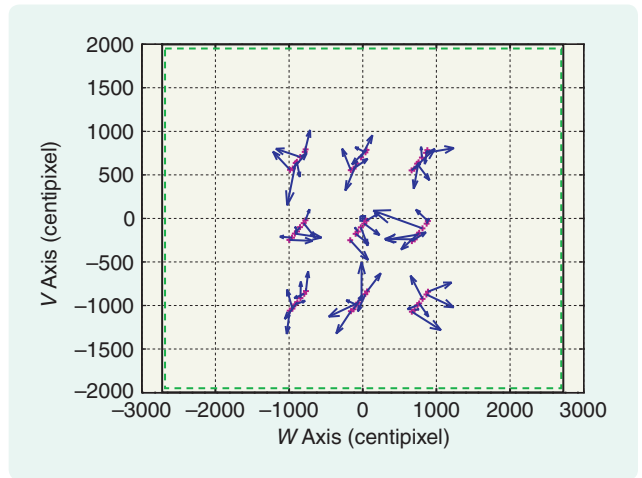


**FIGURE 10** Infrared spectrograph red peak-up array (frame 018) a posteriori prediction error quiver plot in oriented angular pixel coordinates (centipixels). Quivers point from the a posteriori prediction to the corresponding centroid measurement and are magnified by a factor of 100. Small quiver sizes indicate that errors are reduced, while randomness in quiver size and direction indicates that the systematic errors are removed and the residual is effectively whitened by the estimation process. The dashed outer box indicates the nominal array size of  $1 \times 1.2$  arcmin as projected onto the celestial sphere. The solid outer box indicates the estimated array size after calibration.

32 times, and the final data set consists of a total of 192 science centroids and 224 PCRS measurements. The IPF filter estimates 18 parameters including one constant plate scale along the cross-dispersion direction and two IPF alignment angles. The dispersion direction of a rectangular slit is defined along its shorter dimension.

A priori predictions versus measurements are shown in Figure 13, and a posteriori predictions versus measurements

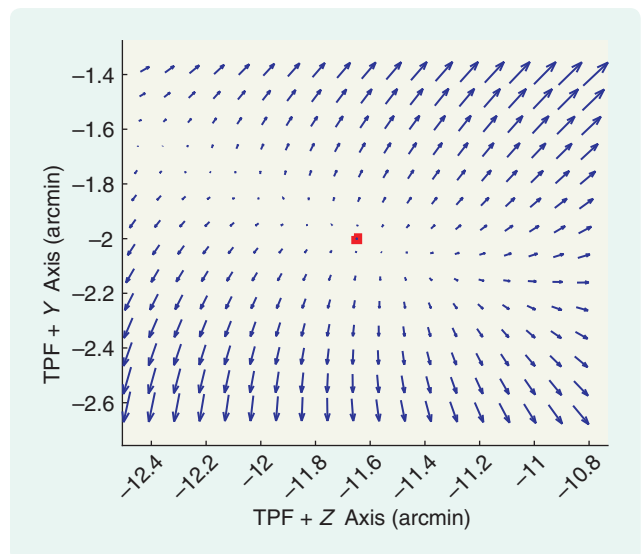


**FIGURE 11** Infrared spectrograph red peak-up array (frame 018) optical distortion plot with quivers magnified by a factor of five. The quivers indicate the direction and amount of local stretching required to map an undistorted array to the observed optically distorted array.

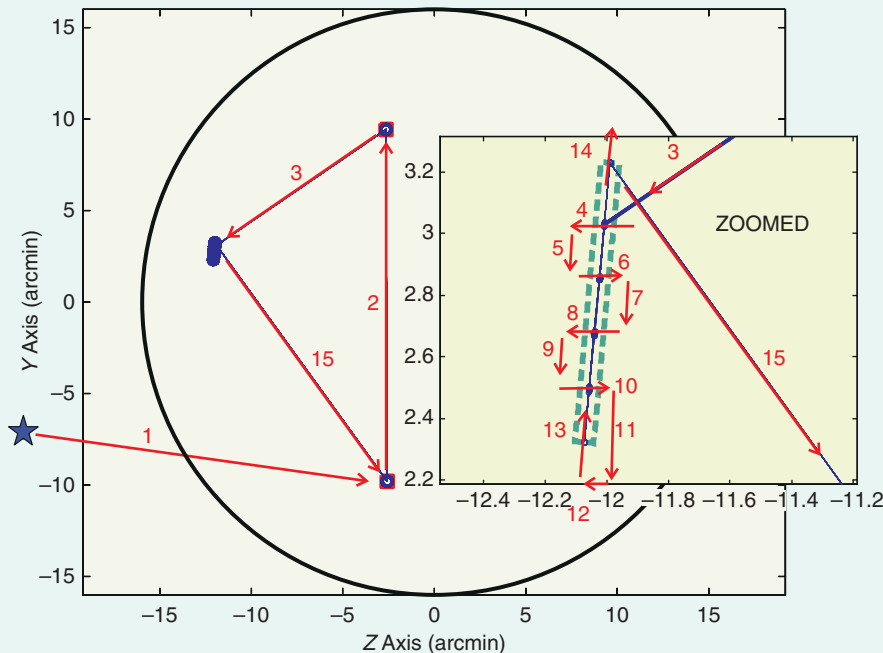


**FIGURE 12** Sandwich maneuver for calibrating the infrared spectrograph (IRS) short-lo slit. The maneuver places a star image on PCRS1 (leg 1), moves the image to PCRS2 (leg 2), moves the image to the IRS short-lo slit (leg 3), and then moves the image across the slit four times back and forth in the dispersion direction (legs 4-11 shown in zoomed insert). Next, the maneuver moves the star image once across in the cross-dispersion direction (legs 13, 14), and finally, back to PCRS1 (leg 15).

are shown in Figure 14. The frame calibration is accurate to 0.1165 arcsec, satisfying its fine survey requirement of 0.14 arcsec.

### Case Study 3: IRAC 3.6- $\mu\text{m}$ Array (Frame 068)

The IRAC 3.6- $\mu\text{m}$  array is calibrated based on the sandwich maneuver shown in Figure 15. This maneuver is repeated four times, and the final data set consists of a total of 1473 IRAC science centroids and 148 PCRS centroids. The filter estimates 21 parameters including three constant and six linear plate scales. The pixel size is nominally 1.21 arcsec as projected onto the celestial sphere.

A priori prediction errors are plotted as quivers in Figure 16. A posteriori prediction errors are plotted as quivers in Figure 17. The Kalman filter residuals are plotted as histograms in Figure 18, and an optical distortion plot is depicted in Figure 19. The frame calibration is accurate to 0.09 arcsec, satisfying its fine survey requirement of 0.14 arcsec.

### Case Study 4: MIPS 24- $\mu\text{m}$ Array (Frame 095)

The MIPS 24- $\mu\text{m}$  array is calibrated based on the series of seven sandwich maneuvers shown in Figure 20. This series is repeated twice and consists of a total of 460 science centroids and 126 PCRS measurements. The IPF filter estimates 33 parameters including three constant and six linear plate scales, four  $\Gamma$ -dependent parameters, and two scan-mirror parameters. The pixel size is nominally 2.5 arcsec as projected onto the celestial sphere.

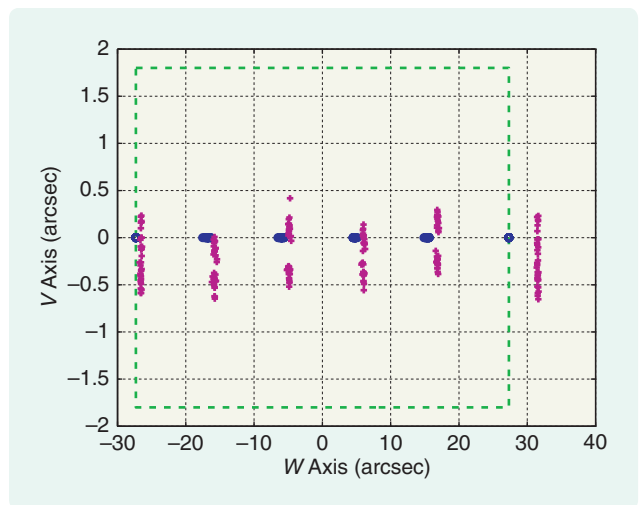


**FIGURE 13** Infrared spectrograph short-lo slit (frame 028) a priori predictions versus measurements in oriented angular pixel coordinates with measurements (o), and a priori predictions (+). The IRS measurements are pseudocentroids that fall on the slit centerline due to a special construction. For IRS spectroscopy slits, centroids are not available in a conventional sense. Instead, a pseudocentroid is defined by reporting the source to be at the slit center at the time of maximum total flux. Determining this time involves fitting a quadratic to the measured total flux as a function of time, and interpolating to find the time of maximum total flux. The pseudocentroid contains information only in the dispersion direction. The dashed outer box indicates the nominal slit size of  $3.6 \times 57$  arcsec as projected onto the celestial sphere (aspect ratio not to scale).

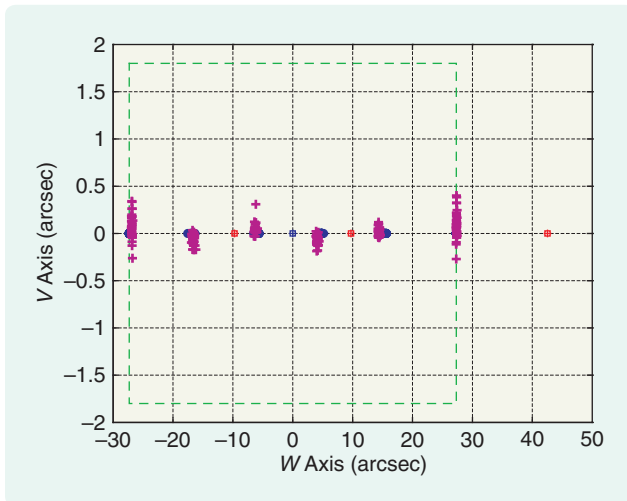


**FIGURE 14** Infrared spectrograph short-lo slit (frame 028) a posteriori predictions versus measurements in oriented angular pixel coordinates with measurements (o), and a priori predictions (+). The vertical displacements seen in the a posteriori predictions are due to systematic errors in the pseudocentering process. These errors can be compared in size to the slit dimensions indicated by the dashed lines.

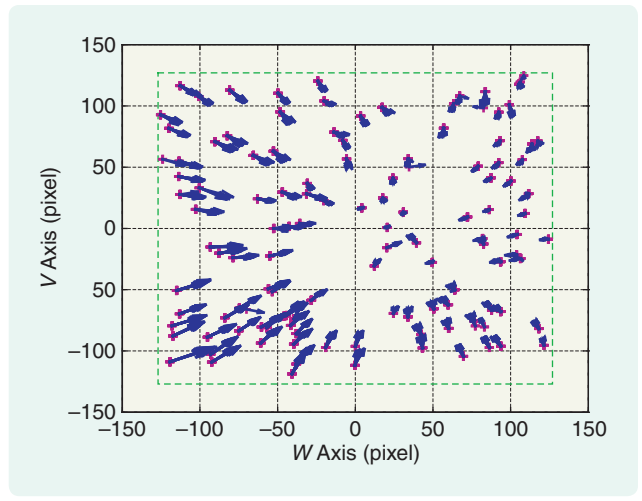


**FIGURE 16** Infrared array camera 3.6- $\mu\text{m}$  array (frame 068) a priori prediction error quiver plot in oriented angular pixel coordinates (pixels). Quivers point from the a priori prediction to the corresponding centroid measurement and are magnified by a factor of ten. Long quivers pointing toward the center of the array indicate systematic errors. The dashed outer box indicates the nominal array size of  $5.2 \times 5.2$  arcmin as projected onto the celestial sphere.

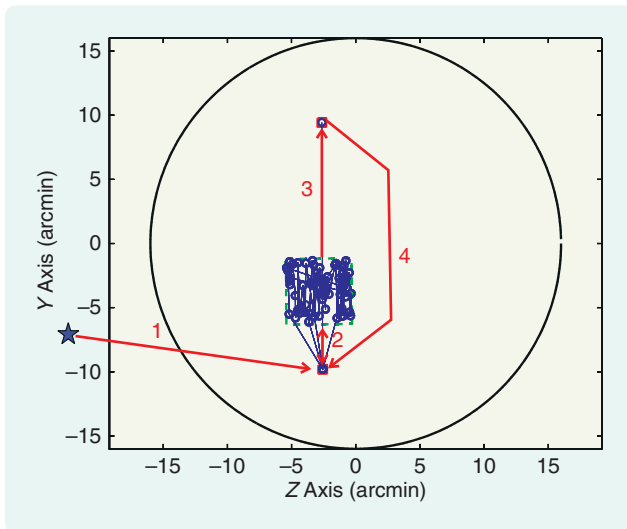


**FIGURE 15** Sandwich maneuver for calibrating the infrared array camera 3.6- $\mu\text{m}$  array. The maneuver places a calibration star image on PCRS1 (leg 1), simultaneously images a cluster of stars on the IRAC 3.6- $\mu\text{m}$  array, and then dithers the cluster to several positions to obtain additional centroids on both the array and PCRS1 (leg 2). The calibration star image is then moved to PCRS2, and the cluster is again dithered to obtain additional centroids on both the array and PCRS2 (leg 3). Finally, the calibration star image is moved back to PCRS1 to obtain only PCRS1 centroids (leg 4). After this procedure, the entire maneuver is repeated four times.

A priori prediction errors are plotted as quivers in Figure 21, and a posteriori prediction errors are plotted as quivers in Figure 22. Calibration results indicate that corrections made to constant plate scale parameters are on the order of one part in a thousand, with significant corrections made

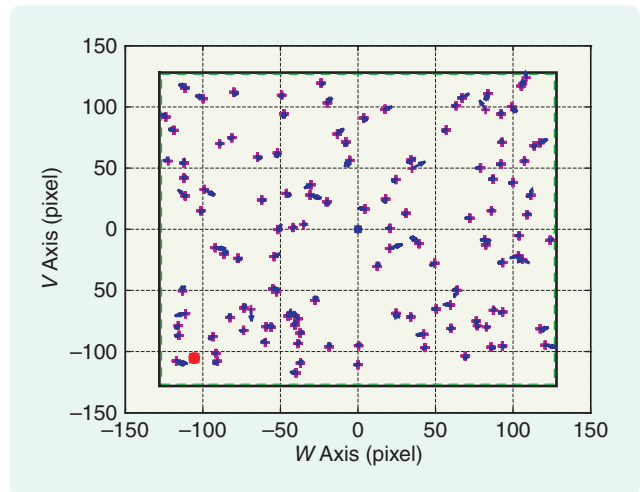


**FIGURE 17** Infrared array camera 3.6- $\mu\text{m}$  array (frame 068) a posteriori prediction error quiver plot in oriented angular pixel coordinates (pixels). Quivers point from the a posteriori prediction to the corresponding centroid measurement and are magnified by a factor of ten. Small quiver sizes indicate that errors are reduced, while randomness in quiver size and direction indicates that the systematic errors are removed and the residual is effectively whitened by the estimation process. The dashed outer box indicates the nominal array size of  $5.2 \times 5.2$  arcmin as projected onto the celestial sphere. The solid outer box indicates the estimated array size after calibration.

to compensate high-order-optical distortions. Corrections of approximately 4% are made to the scan mirror scale-factor and a 0.7-degree misalignment correction is made with respect to the orientation of the 24- $\mu\text{m}$  array. The optical distortions estimated by the IPF Kalman filter at

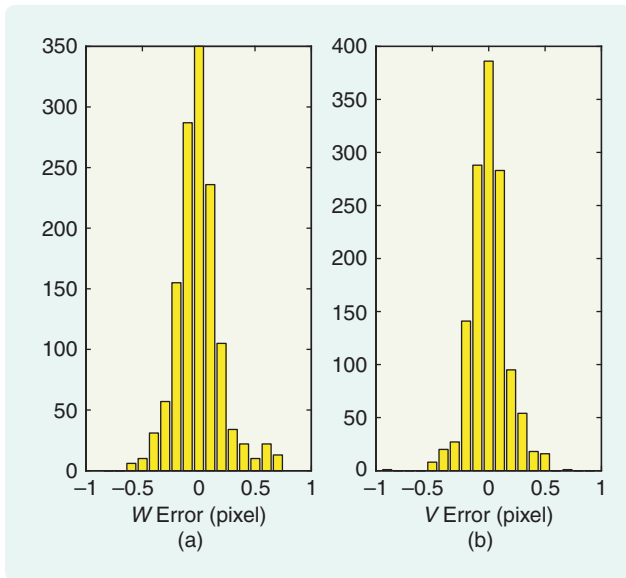


**FIGURE 18** Infrared array camera 3.6- $\mu\text{m}$  array (frame 068) Kalman filter innovations. (a) Histogram of innovations along the  $w$ -axis (pixels). (b) Histogram of innovations along the  $v$ -axis (pixels), where the pixel is 1.21 arcsec. The general health of the calibration process is diagnosed by the size and whiteness of the innovations process. The removal of systematic errors is evidenced by the lack of spikes and other artifacts. The innovation's sub-pixel size is consistent with expected IRAC centroiding errors.

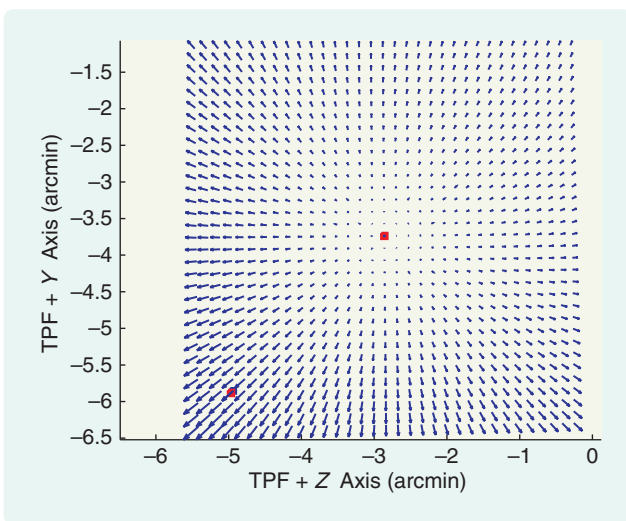


**FIGURE 19** Infrared array camera 3.6- $\mu\text{m}$  array (frame 068) optical distortion plot with quivers magnified by a factor of five. Quivers indicate a bowl-shaped distortion, which is largest at the lower-left-hand corner of the array.

zero scan-mirror offset are plotted in the quiver plot Figure 23. As a comparison, optical distortions obtained using a purely physical modeling approach based on the Code V ray-tracing program are shown in Figure 24. Agreement between quiver direction and relative size provides an independent check on the general shape of the optical

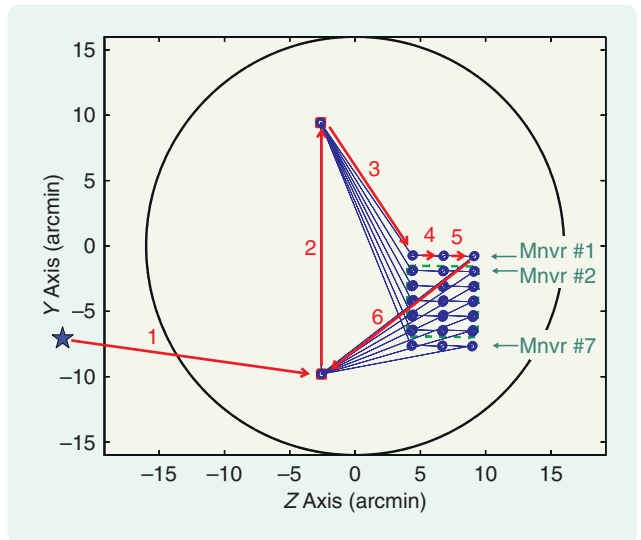


**FIGURE 20** Sandwich maneuver for calibrating the multiband imaging photometer for Spitzer 24- $\mu\text{m}$  array. This maneuver produces a 7-by-3 grid of observations, where each row of three observations uses a separate sandwich maneuver. For each point in a given row the spacecraft attitude is fixed, and there are seven scan mirror positions based on moving the source three positions up and three positions down from its nominal position in approximately 25-arcsec increments. Centroids that fall off the array are not recorded.

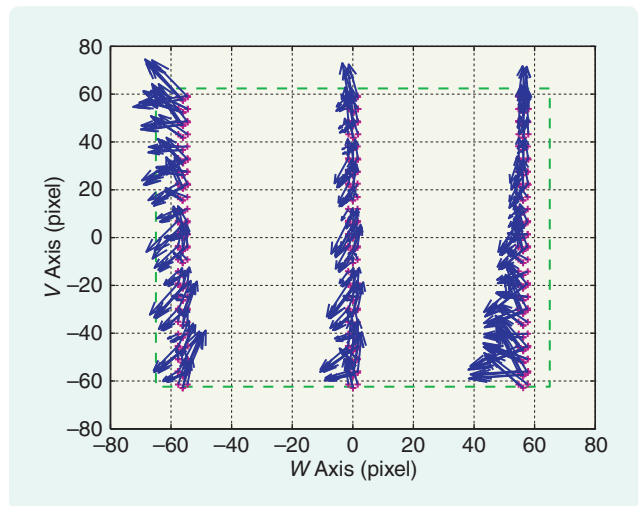


**FIGURE 21** Multiband imaging photometer for Spitzer 24- $\mu\text{m}$  array (frame 095) a priori prediction error quiver plot in oriented angular pixel coordinates (pixels). Quivers point from the a priori prediction to the corresponding centroid measurement, and are magnified by a factor of ten. Groups of long arrows pointing in similar directions indicate systematic errors. The dashed outer box indicates the nominal array size of  $5.4 \times 5.4$  arcmin as projected onto the celestial sphere.

distortion pattern. Focal-plane calibration accuracy is 0.09 arcsec meeting the 0.14 arcsec requirement.

## DISCUSSION

The integrated high-order Kalman implementation represents a technological advance with respect to aerospace

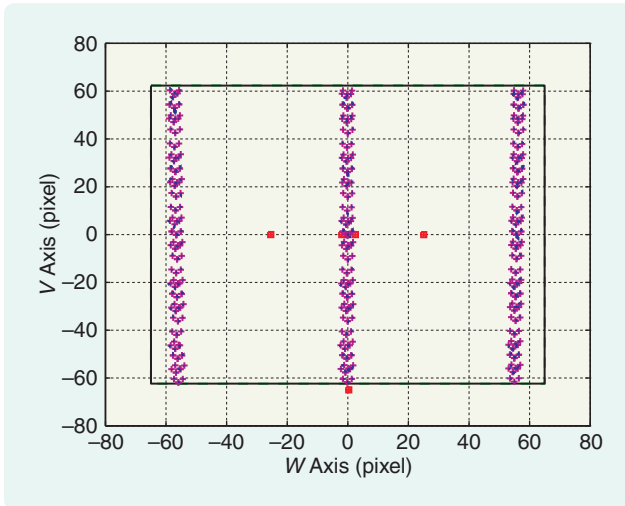


**FIGURE 22** Multiband imaging photometer for Spitzer 24- $\mu\text{m}$  array (frame 095) a posteriori prediction error quiver plot in oriented angular pixel coordinates (pixels). Quivers point from the a posteriori prediction to the corresponding centroid measurement, and are magnified by a factor of ten. Small quiver sizes indicate that errors are reduced, while randomness in quiver size and direction indicates that the systematic errors are removed and the residual is effectively whitened by the estimation process. The dashed outer box indicates the nominal array size of  $5.4 \times 5.4$  arcmin as projected onto the celestial sphere. The solid outer box indicates the estimated array size after calibration.

tradition that dictates breaking the calibration problem into subsets of parameters and estimating them separately. Typically, frame alignments are estimated separately from optical distortions in separate filters and by separate teams of analysts. Breaking the problem up allows programmatic simplifications since engineering and science teams can work largely independently. However, the practice of breaking up

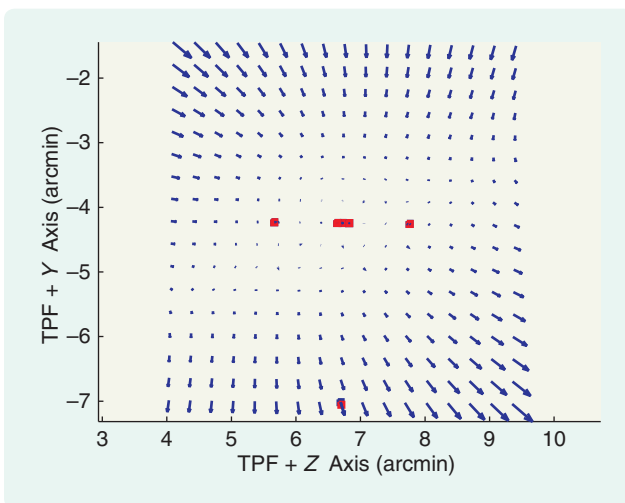


**FIGURE 23** Multiband imaging photometer for Spitzer 24- $\mu\text{m}$  array (frame 095) optical distortion plot with quivers magnified by a factor of five. Quivers indicate pixel compression at the top of the array and pixel expansion at the bottom.

the calibration problem also has serious technical limitations. One limitation is that the theory becomes ad hoc and estimation results are no longer optimal. A second limitation is that many advantages of using modern filter theory are lost. Joint statistics are not available, and a wealth of diagnostics and health monitoring approaches are not applicable. Furthermore, the lack of joint statistics makes it impossible to do a proper covariance analysis to predict performance of the calibration process beforehand, and there is little recourse when things go wrong after the fact. Specific advantages of the integrated calibration approach in overcoming these limitations for Spitzer are outlined below.

The a posteriori joint covariance matrix from the integrated Kalman filter is indispensable for preflight design of calibration experiments. Based on the joint covariance matrix, sandwich maneuvers are designed so that key calibration parameters are observable, and the number of repetitions is sufficient to ensure that parameters are calibrated to the required accuracy [22]. This experiment design process is not possible when the calibration problem is broken up since a joint covariance matrix is not available.

The integrated calibration process is streamlined and time efficient compared to traditional approaches that require additional steps of iterating between teams of analysts. Time-efficiency is particularly relevant to IR missions such as Spitzer, whose total lifetime is defined by expenditure of its finite cryogen resources.

Despite best efforts, there are sometimes redundant parameters left in the calibration parameterization. Redundant parameters are unwanted because they cannot be

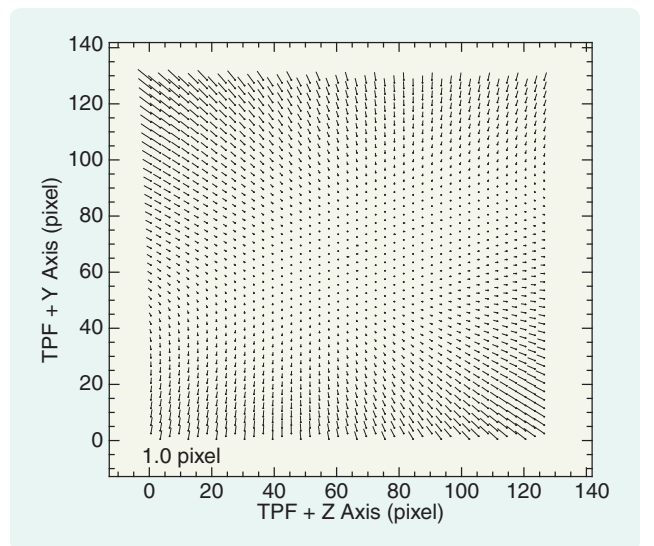


**FIGURE 24** Multiband imaging photometer for Spitzer 24- $\mu\text{m}$  array (frame 095) optical distortion plot based on analysis using the Code V ray-tracing program (adapted from the work of Jane Morrison, University of Arizona). Agreement between quiver direction and relative size provides an independent check on the general shape of the optical distortion pattern obtained by the instrument pointing frame Kalman filter results in Figure 23.

uniquely identified. When the calibration problem is broken up, parameter redundancies can go undetected and cause undesirable instabilities in the parameter estimates [10]. On the other hand, parameter redundancies are easily detected in the integrated calibration approach by the presence of large diagonal entries and strong associated off-diagonal entries seen in the joint covariance matrix. Once detected, redundancies are generally physically interpretable and easily removed.

IPF Kalman filter residual tests are critical for diagnosing a wide range of systematic errors entering into the pointing chain. These errors include units errors, polarity errors, non-IPF filter-related calibration errors, and errors from unexpected changes in pointing chain elements. Kalman filter residual tests are not possible when the calibration problem is broken up.

The IPF filter is designed as a variable-dimension filter that supports masking out extraneous parameters. The masking feature simplifies the process of finding accurate reduced-order models. A systematic approach is to start with models having few parameters and then add parameters until standard Kalman filter residual tests are met. Without residuals, it would be impossible to properly guide this order-reduction process.

In the IPF filter processing, the covariance of the measurement noise is chosen as  $\text{cov}(\tilde{n}) = \sigma^2 \tilde{R}$ , where  $\sigma^2$  is an additional scale factor estimated from data using the sum-squared Kalman-filter residuals. This technique, borrowed from the least-squares literature [23], rescales covariances based on actual measured residuals, and provides an improved assessment of calibration-error covariances. This noise rescaling approach is not possible if the calibration problem is broken up.

The integrated calibration approach enables powerful data pruning methods to be developed based on a posteriori filter residuals. The idea is to first perform an initial IPF filter run and then make a two-dimensional plot of the a posteriori residuals. Outliers are clearly seen in this plot, and decisions can be made to remove specific centroids based on imposing statistical thresholds. An example is the IRAC calibration, where entire star clusters are centroided. Despite best efforts, centroids are occasionally associated with incorrect catalog stars. The pruning method is able to catch the resulting incorrect associations very effectively.

## CONCLUSIONS

A 37-state IPF Kalman filter is used to calibrate the Spitzer telescope focal plane. The high-order filter enables, for the first time, an integrated approach to focal-plane calibration, where science and engineering parameters are estimated in the same filter. The Spitzer application demonstrates that the integrated approach offers significant advantages with respect to optimality, time-efficiency, anomaly detection, and health monitoring compared to

existing telescope-calibration approaches, where the parameters are artificially broken into subsets that are estimated by separate teams of analysts. Performance results for the IPF Kalman filter indicate that all Spitzer calibration requirements are satisfied, and are consistent with margins predicted by preflight error analysis.

On a final note, after more than five-and-a-half years of probing the cool cosmos, Spitzer entered standby mode on May 15, 2009, as a result of running out of the liquid helium coolant that kept its infrared instruments chilled. This event marks the successful completion of the Spitzer's cold mission as originally commissioned by NASA. However, even though the telescope is warming up, the IRAC arrays continue to operate and provide useful scientific data. A new follow-on warm mission based on the IRAC arrays has been defined and initiated, so that Spitzer will remain in commission for several years to come.

## ACKNOWLEDGMENTS

This work was performed at the Jet Propulsion Laboratory, California Institute of Technology, under contract with the National Aeronautics and Space Administration. The focal-plane survey was a highly collaborative effort, and the authors acknowledge the entire Spitzer project and the close participation of various engineering and science teams, namely Jocelyn Keene, Bill Wheaton, Jane Morrison (MIPS), Peter Eisenhardt, Sean Carey (IRAC), Carl Grillmair, Keven Uchida, Bernhard Brandl (IRS), Elmain Martinez, Myche McAuley (MIPL), Amy Mainzer (PCRS), Dan Swanson, Chris Voth, Dave Eckart, Angus McMechen (OET, Lockheed-Martin), John Gilbert, John Miles (IOC/SV planning), Keyur Patel, Bob Wilson (flight system), Fernando Tolivar, Tooraj Kia, Johnny Kwok, Mike Werner, Charles Lawrence, Nick Gautier, Jeff Van Cleve, and Bill Mahoney (consultations, scientific and technical advice).

## AUTHOR INFORMATION

*David S. Bayard* (david.bayard@jpl.nasa.gov) received a B.A. degree in mathematics from Queens College of the City University of New York in 1977 and the M.S. and Ph.D. degrees in electrical engineering from the State University of New York at Stony Brook in 1979 and 1984, respectively. He is currently a senior research scientist at the Jet Propulsion Laboratory, California Institute of Technology. His work includes over 150 papers in refereed journals and conferences, 50 NASA Tech Brief Awards, and three U.S. patents. In 2005, he was awarded the NASA Exceptional Engineering Achievement Medal for contributions to the Spitzer Space Telescope pointing control system, and in 2006 he received the American Automatic Control Council (AACC) Control Engineering Practice Award. He is a member of IEEE, SIAM, AIAA, Phi Beta Kappa, and Beta Delta Chi. He can be contacted at MS 198-326, Jet Propulsion Laboratory, 4800 Oak Grove Drive, Pasadena, CA 91109 USA.

**Bryan H. Kang** received a B.S. degree in aerospace engineering from the University of Southern California in 1987 and the S.M. and Ph.D. degrees from the Massachusetts Institute of Technology, Department of Aeronautics and Astronautics, in 1989 and 1995, respectively. He is currently a GN&C manager for the Soil Moisture Active-Passive mission at the Jet Propulsion Laboratory, California Institute of Technology. He has worked for various research and flight projects including the Space Interferometry Mission, Spitzer Telescope, TES instrument, and Formation Flying Research. Previously he worked at TRW as a GN&C technical staff supporting the EOS Aqua/Aura and KOMPSAT projects. His areas of specialization include nonlinear estimation and precision control for space and optical applications.

**Paul B. Brugarolas** is a senior engineer at the Jet Propulsion Laboratory. He received the electrical engineer degree from the University of Navarre, San Sebastian, Spain, and the M.S. and Ph.D. degrees in electrical engineering from the University of Southern California, Los Angeles. He joined the Guidance and Control Analysis Group at the Jet Propulsion Laboratory in 1997. He is currently designing the entry attitude controller for the Mars Science Laboratory. His research interests include robust control, estimation theory, system identification, and model validation. He received the NASA Exceptional Achievement Medal for contributions to the Shuttle Radar Topography Mission. He is a Senior Member of the IEEE and AIAA.

**Dhemitrios Boussalis** received the Ph.D. degree in electrical engineering from New Mexico State University in 1979. He was a research associate and assistant professor with the Department of Electrical Engineering at NMSU until 1980 when he joined the Guidance and Control section at the Jet Propulsion Laboratory, where he is a member of the technical staff. He has conducted research on precision pointing systems, adaptive attitude/vibration control of flexible space platforms, and developed neural network concepts and algorithms with application to adaptive/autonomous spacecraft control. His current research includes the development of control and error analysis algorithms related to space interferometers and precision pointing mirrors. He is a member of Eta Kappa Nu, IEEE, and AIAA.

## REFERENCES

- [1] *Spitzer Science Center, California Institute of Technology* (2009) [Online]. Available: <http://www.spitzer.caltech.edu>
- [2] D. S. Bayard, "Spacecraft pointing control criteria for high resolution spectroscopy," *IEEE Trans. Aerosp. Electron. Syst.*, vol. 35, no. 2, pp. 637-644, Apr. 1999.
- [3] D. S. Bayard, "Advances in precision pointing control for the NASA Spitzer Space Telescope," *Adv. Astronaut. Sci.*, AAS Paper AAS 04-071, vol. 118, pp. 527-546, 2004.
- [4] D. S. Bayard and B. H. Kang, "A high-order Kalman filter for focal plane calibration of NASA's space infrared telescope facility (SIRTF)," in *Proc. AIAA Guidance, Navigation and Control Conf. and Exhibit*, Austin, TX, Aug. 11-14, 2003, Paper # AIAA-2003-5824.
- [5] D. S. Bayard, B. H. Kang, P. B. Brugarolas, and D. Boussalis, "An integrated optimal estimation approach to Spitzer Space Telescope focal plane survey," in *Proc. SPIE Conf. Astronomical Telescopes and Instrumentation*, Glasgow, Scotland, U.K., June 21-25, 2004, Paper # 5487-84.
- [6] D. S. Bayard and B. H. Kang. (2004, June 30). *SIRTF instrument pointing frame (IPF) Kalman filter algorithm*. JPL D-Document D-24809 [Online]. Available: <http://hdl.handle.net/2014/41281>
- [7] J. W. Murrell, "Precision attitude determination for multimission spacecraft," in *Proc. AIAA Guidance and Control Conf.*, Palo Alto, CA, Aug. 7-9, 1978, Paper No. 78-1248.
- [8] D. B. Reid, "Calibration of the MILSTAR attitude determination system," in *Proc. IEEE American Control Conf.*, Albuquerque, NM, June 1997, pp. 557-563.
- [9] M. C. Zanardi and M. D. Shuster, "Batch, sequential and hybrid approaches to spacecraft sensor alignment estimation," *J. Astronaut. Sci.*, vol. 51, no. 3, pp. 279-290, 2003.
- [10] R. V. F. Lopes and M. D. Shuster, "Parameter interference in distortion and alignment calibration," *J. Astronaut. Sci.*, vol. 51, no. 3, pp. 261-277, 2003.
- [11] M. D. Shuster, G. J. Bierman, and D. S. Pitone, "Batch estimation of spacecraft sensor alignment—I: Relative alignment estimation," *J. Astronaut. Sci.*, vol. 39, no. 4, pp. 519-546, 1991.
- [12] S. Davis and J. Lai, "Attitude sensor calibration for the ocean topography experiment satellite (TOPEX)," in *Proc. SPIE Space Guidance, Control and Tracking Conf.*, vol. 1949. *Society of Photo-Optical Instrumentation Engineers*, 1993, pp. 80-91.
- [13] M. Pittelkau, "Kalman filtering for spacecraft system alignment calibration," *J. Guid., Control Dyn.*, vol. 24, no. 6, pp. 1187-1195, Nov./Dec. 2001.
- [14] M. Pittelkau, "Survey of calibration algorithms for spacecraft attitude sensors and gyros," in *Proc. AAS/AIAA Astrodynamics Specialist Conf.*, Mackinac Island, MI, Aug. 19-23, 2007, Paper No. AAS 07-295.
- [15] D. S. Bayard, B. H. Kang, P. B. Brugarolas, and D. Boussalis. (2004, July 8). *Spitzer space telescope focal plane survey final report*. Jet Propulsion Lab., Internal Document JPL D-27667 [Online]. Available: <http://hdl.handle.net/2014/41280>
- [16] The International Celestial Reference System (ICRS). *Astronomical Applications Department of the U.S. Naval Observatory* (2009) [Online]. Available: [http://aa.usno.navy.mil/faq/docs/ICRS\\_doc.php](http://aa.usno.navy.mil/faq/docs/ICRS_doc.php)
- [17] P. K. Seidelmann, *Explanatory Supplement to the Astronomical Almanac*. Sausalito, CA: Univ. Science Books, 1992.
- [18] B. M. Bell and F. W. Cathey, "The iterated Kalman filter update as a Gauss-Newton method," *IEEE Trans. Automat. Contr.*, vol. 38, no. 2, pp. 294-297, Feb. 1993.
- [19] T. Kailath, A. H. Sayed, and B. Hassibi, *Linear Estimation*. Upper Saddle River, NJ: Prentice Hall, 1999, pp. 433-444.
- [20] J. P. Schwenker, B. R. Brandl, W. Burmester, J. Hora, A. K. Mainzer, P. C. Quigley, and J. Van Cleve, "SIRTF-CTA optical performance test," *Proc. SPIE*, vol. 4850, pp. 304-317, 2003.
- [21] J. P. Schwenker, B. R. Brandl, W. F. Hoffman, J. Hora, A. K. Mainzer, J. E. Mentzell, and J. Van Cleve, "SIRTF-CTA optical performance test results," *Proc. SPIE*, vol. 4850, pp. 30-41, 2003.
- [22] D. S. Bayard, P. B. Brugarolas, D. Boussalis, and B. H. Kang. (2003, Sept. 1). SIRTF focal plane survey: A pre-flight error analysis. JPL D-26678 [Online]. Available: <http://hdl.handle.net/2014/41147>
- [23] G. A. F. Seber, *Linear Regression Analysis*. New York: Wiley, 1977, pp. 51-54.

